ACKNOWLEDGEMENT

I would like to express my sincere appreciation to my advisors Prof. Dr. A Rüstem Aslan and Assoc. Prof. Dr. Firat Oğuz Edis for their valuable guidance and support during the entire of this study.

I also extend thanks to ROTAM employees for their valuable contributions.

Finally, I would like to take this opportunity to express my deepest love, appreciation, and gratitude to my family for their continuous support and encouragement. Especially, to my sister Kader Yağız (MSc) who always encourages me from the beginning to the end of this study.

January, 2005 Bedri YAĞIZ

TABLE OF CONTENTS

LIST OF TABLES

LIST OF FIGURES

LIST OF SYMBOLS

M_t : Blade tip Mach number $M_{tip} = \dfrac{V_{tip}}{a_\infty}$

C_T : Thrust coefficient $C_T = \dfrac{T}{\rho(\pi R^2)(\Omega R)^2}$

N : Blade Number

R : Blade Radius (mm)

r : Distance between boundary cell face and hub (mm)

W_e : Outflow boundary Mach number

W_i : Inflow boundary Mach number

C_l : Lift Coefficient $C_L = \dfrac{L}{\rho V^2 S / 2}$

Θ_c : Rotor collective angle (degree)

C_p : Pressure Distribution $C_P = \dfrac{p - p_\infty}{\rho V^2 / 2}$

G_v : Production of turbulent viscosity

Y_v : Destruction of turbulent viscosity

v : Molecular kinematic viscosity

σ_V : Constant (page 17)

C_{b2} : Constant (page 17)

C_{b1} : Constant (page 17)

k : Constant (page 18)

S_v : User-defined source term

d : Distance from the wall

S : Scalar measure of the deformation tensor

ROTOR PALA UCU ŞEKLİNİN HELİKOPTER PERFORMANSINA ETKİSİ

ÖZET

Helikopter, döner kanat kullanarak taşıma, itki ve kontrol sağlayan bir hava aracıdır. Döner kanatlar, uçuşu sürdürebilmek için havanın öteleme hızına ihtiyacı olan sabit kanatlı uçakların aksine aracın hızı sıfır olsa dahi kanat yüzeyinin havaya göre olan hareketinden dolayı aerodinamik kuvvetler üretirler. Böylelikle helikopterler dikey uçuş kabiliyetine sahip olurlar.

Modern helikopter tasarımında rotor etrafındaki akış alanının öngörümü önem arz eder. CFD analizleri rotor aerodinamik performansının hesaplanmasında çok yönlüdür. Rotor etrafındaki akış lineer olmayan, üç boyutlu ve bir önceki palanın bozuntu oluşturduğu akış alanında hareket eden paladan dolayı artan bir kararsızlığa sahiptir.

Gelişmiş rotor teknolojisinde geleneksel olmayan kanat profillerinin kullanılması yönünde yapılan araştırmalar, yeni nesil helikopterlerin ihtiyaçlarını sağlamak için temel ilgi alanını oluşturur. Bu ihtiyaçlar taşıma kabiliyetinin, menzilin ve dayanıklılığın arttırılması, yüksek ileri uçuş hızı, yüksek manevra yeteneği ve çeviklik sağlamak olarak sıralanabilir. Özellikle sivil uygulamalar için gürültü yayılımının azaltılması ilgi alanıdır.

Bu çalışmada helikopterin askı durumundaki rotor palalarının sayısal çözümlemesi yapılmıştır. CFD yazılımı olan Fluent 6.1 programı kullanılarak üç boyutlu helikopter palalarının etrafındaki akış incelenmiştir. Rotor palaları burulmasız, incelme olamayan, altı birim kanat açıklığına sahip ve tek kanat profilinden (NACA0012, VR7) oluşturulmuştur. Hesaplamalar farklı uç hızlarında (M_t=0.439 ve 0.877) ve kollektif açılarında (Θ_c=0^0 ve 8^0) değişik akış koşulları için yapılmıştır. Son olarak, kare, daralmalı (tapered) ve geriye süpürmeli (swept), tek NACA2415 profilinden oluşan üç farklı uç şekline sahip pala geometrileri kullanılmıştır. Pala geometrileri CATIA V5R12 programında çizilmiş ve Gridgen V15 programı kullanılarakta ağ alanı oluşturulmuştur.

EFFECT OF ROTOR BLADE TIP SHAPE ON HELICOTER MAIN-ROTOR PERFORMANCE

SUMMARY

A helicopter is an aircraft that uses rotating wings to provide lift, propulsion, and control. The rotary wings can produce aerodynamics forces, which are generated by the relative motion of a wing surface with respect to the air, even when the velocity of the vehicle itself is zero, in contrast to fixed-wing aircraft, which needs a translational velocity to maintain flight. Hence, the helicopter has the ability of vertical flight, including vertical take-off and landing.

The prediction of the flow field around a rotor has an important part in modern helicopter design. CFD analysis is so versatile to analysis of the rotor aerodynamic performance, which can be used to investigate the flow about almost any type of vehicle, including rotorcraft. The flow is non linear highly three dimensional, and unsteadiness is increased due to each blade moving into a fluid which has already been disturbed by a previous blade

Research on using unconventional airfoils for advanced rotor technology has been of primary interest to meet the requirements of a next generation rotorcraft. These requirements are increased payload capability, and range and endurance, higher forward flight speed, and greater maneuverability and agility. Reduced noise emission is also of interest, particularly for civilian applications.

In this study, numerical solutions of the helicopter rotor blades in hover have been carried out. The flow field around the three dimensional helicopter rotor blades is investigated by using CFD software, FLUENT 6.1. The rotor blades with no twist or taper, aspect ratio six, with a single NACA0012 and VR7 airfoils were chosen. The computations are obtained for various flow conditions with different tip Mach numbers (M_t=0.439 and 0.877) and collective pitch settings ($\Theta_0=0^0$ and 8^0). Finally, three different blade geometries are generated by a single NACA2415 airfoil with different blade tip shapes including square, tapered, and swept. The blade geometries were drawn by using CATIA V5R12 program and their computational domains were generated by Gridgen grid generation software.

1. INTRODUCTION

1.1 Physical Background

Igor Sikorsky's vision of a rotating wing aircraft that could safely hover and perform other desirable flight maneuvers under full control of the pilot was only to be achieved some thirty years after fixed-wing aircraft (airplanes) were flying successfully. This rotating-wing aircraft we know today as the helicopter [1]. A helicopter is an aircraft that uses rotating wings to generate aerodynamic lift equal in magnitude to the helicopter weight, a propulsive force needed to overcome vehicle drag in forward flight and maneuvers, forces and moments needed to control the altitude and position of the helicopter. The rotary wings can produce aerodynamic forces, which are generated by the relative motion of a wing surface with respect to the air, even when the velocity of the vehicle itself is zero, in contrast to fixed-wing aircraft, which needs a translational velocity to maintain flight. Hence, the helicopter has the ability of vertical flight, including vertical take-off and landing. Compared to fixed wing flight, the development of which can be clearly traced to Lilientha, Langley, and the first fully controlled flight of a piloted powered aircraft by the Wight Brothers in 1903, the origins of successful helicopter flight are less clear [1]. However, when compared to fixed-wing aircraft, there are many evolution of the helicopter. Moreover, also this growth period of the helicopter require greater depth of scientific and aeronautical knowledge.

The conventional helicopter rotor consists of two or more identical, equally spaced blades attached to a central hub. The blades are maintained in uniform rotational motion, usually by a shaft torque from the engine. The power transmitted to the rotor shaft is the relatively low amount of power required to lift the machine compared to a fixed-wing aircraft of the same gross weight. The lift and drag forces on these rotating wings produce the torque, thrust and other forces and moments of the rotor [2].

The prediction of the flow field around a rotor has an important part in modern helicopter design. CFD analysis is so versatile to analysis of the rotor aerodynamic performance, which can be used to investigate the flow about almost any type of vehicle, including rotorcraft. The flow is non linear highly three dimensional, and unsteadiness is increased due to each blade moving into a fluid which has already been disturbed by a previous blade. However, hovering flight can be simulated as a steady solution in a moving frame [5].

Because of the proximity of the wake of a helicopter to the rotor disk, modeling the wake structure is vigorous to accurately predict the downwash in the plane of the rotor disk. In radial direction, the blade rotation causes a non-uniform distribution of the velocity field. This generates a high concentration of lift over the outer portion of the blades. Since the physical lift must vanish at the extreme edges of the blades, a high spanwise lift gradient exists near the tip. As a result, strong trailing vortices originate at the tip, which roll up to form concentrated tip vortices a few chord lengths downstream the blades, dominating the rotor wake as illustrated in Figure 1.1.

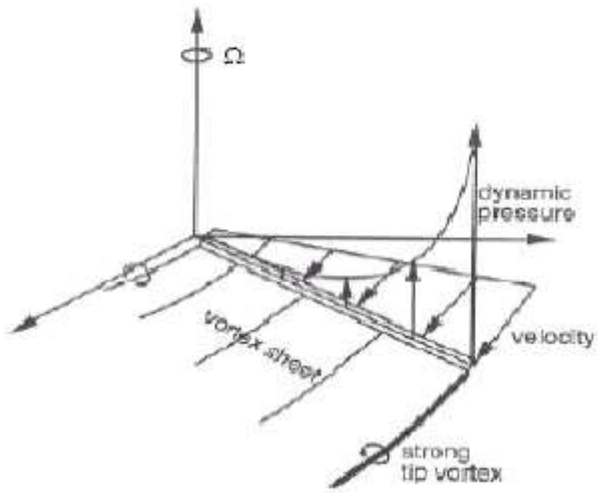

Figure 1.1 Formation of the Tip Vortex [35]

The blade loads and overall performance of the rotor system are highly dependent upon the strengths and locations of the tip vortices relative to the rotor. In addition, during descending low-speed forward flight, blade-vortex interaction (BVI) results in locally large unsteady air loads on the blades, leading to increased rotor vibration levels and the generation of impulsive rotor noise [16, 17]. In summary, the blade tips are of considerable importance since they are at the origin of the formation of the tip vortices and they generate most of the rotor drag and noise [18, 19].

1.2 Hover Simulation Methodologies

The earliest methods for modeling rotors based on an extension of Prandtl's lifting line theory for wings. In these techniques, the individual blades were modeled as lifting line vortices, and the wake was modeled as a deformed helix. During, 1970's Gray [23], Landgrebe [24] among others developed a prescribed wake model to define this helical geometry. Their models were based on experimental observations, such as smoke visualization of the wake. Kocurek and Tangler [3] and Shenoy [15] refined the lifting line method by using a lifting surface representation of the rotor with an improved prescribed tip vortex and inner vortex geometry.

Free wake analysis methods were subsequently developed by Scully [25], Summa [26], Bliss and Miller [27] among others. In these methods the tip vortex was modeled as a series of line vortex filaments and was tracked using a Lagrangian technique. The velocity field was computed using the Biot-Savart law and numerical integration techniques. Johnson W [28] used the free wake technique as an option in his computer program CAMRAD (Comprehensive Analytical Model of Rotorcraft Aerodynamics and Dynamics). Caradonna and Isom [29] extended the transonic small disturbance theory which became available during the early 1970's to transonic flow over rotors. This technique allowed a first principle-based study of forward flight conditions and tip effects.

During early 1980's, Chang [30] modified the full potential flow solver FLO22 for isolated wings to model rotors.

During late 1980's, Euler methods matured to a point where calculation of the rotor flowfield in hover and forward flight was feasible. These methods solved the mass, momentum and energy conservation in a time dependent fashion using finite-difference or finite volume methods. These solvers did not include viscous effects that could analyze the transonic flow with non-isentropic shocks.

Wake and Sankar [31] were one of the first few researchers to develop a Navier-Stokes code to analyze rotor flowfields in hover and forward flight. They used a C-H computational grid and a hybrid ADI implicit time marching algorithm.

Mello [32], Berezin [33] and Moulton et al [34] have developed hybrid Navier-Stokes/Full Potential equation based solvers in an effort to reduce the computation time. Here, the computational domain is divided into an inner domain comprising of the body and the near wake and outer domain far from the body. Navier Stokes equations are solved in the inner domain and the full potential equation is solved in the outer domain where viscous effects are negligible.

1.3 Research Objective and Scope

Research on using unconventional airfoils for advanced rotor technology has been of primary interest to meet the requirements of a next generation rotorcraft. These requirements are increased payload capability, and range and endurance, higher forward flight speed, and greater maneuverability and agility. Reduced noise emission is also of interest, particularly for civilian applications.

In the present work, the formation and evolution of tip vortices trailed from helicopter rotor blades are studied numerically for an improved rotorcraft design, using commercially available CFD software [12]. Hover flight conditions for isolated rigid rotors are considered. NACA0012, NACA2415 and VR7 airfoils are used to form rectangular, swept and tapered blade-tip configurations. The computations are obtained for various flow conditions with different tip Mach numbers and collective pitch settings. The results are compared with other numerical [11, 22] and experimental data [19, 4] for validation.

First an untwisted, rectangular planform six aspect ratio blade with NACA 0012 airfoil was chosen to be compared to numerical data from Strawn & Barth [11] and Yang & Zhuang [22]. Strawn and Barth [11] used unstructured-grid Euler solver for computing helicopter aerodynamic flowfields in their study. Yang and Zhuang [22] present an approach for computing the loads of hovering helicopter rotor using the Navier-Stokes equations. Moreover, the results were compared to experimental data from Caradonna and Tung [4]. In that experiment, NACA 0012 profile blades were used in untwisted and untapered planform. Structured grids were produced using in house available software for the analysis. Spalart-Allmaras [12] and Spalart-Allmaras DES [12] turbulence models were used to account for the turbulence effects. The boundary conditions obtained from one dimensional momentum theory [20], required for the rotor analysis is externally fed into the Navier-Stokes solver so as to simulate proximity flow conditions about a rotating rotor. After the validation of methodology for Caradonna & Tung's [4] blade, the airfoil was changed to VR7 to compare the two blades, which have the same properties except airfoils. The comparison was shown in the Table 7.2 and discussed in the results section.

The second purpose of this study was to show how the blade-tip configurations affect the performance of the rotor. Leishman and Martin [14] examined the wake aerodynamics of a single helicopter rotor blade with several tip shapes including rectangular, swept and tapered, on a hover test stand. The planforms tested in these experiments included a 20^0 swept tip, tapered with a 0.4 taper ratio and rectangular one. The blade parameters and test conditions are given in Table 5.1. Leishman and Martin [14] used a single helicopter rotor blade with a balanced weight for correspondence of loads. However, in the present study 2 blade configurations are modeled in a similar manner to other computations. Unstructured mixed grids were produced using commercially available software [21] for the analysis. Standard k-ε [12] turbulence model is used to account for the turbulence effects. The boundary conditions obtained from one dimensional momentum theory [20]. The computations were performed on a 24 processor SGI O3000 high performance computing system.

2. HELICOPTERS' COMPONENTS

A helicopter is an aircraft that uses rotating wings to generate aerodynamic lift equal in magnitude to the helicopter weight, a propulsive force needed to overcome vehicle drag in forward flight and maneuvers, forces and moments needed to control the attitude and position of the helicopter. Figure 2.1 illustrates the principal helicopter configuration.

In this figure some of the component parts are shown that make up a helicopter. While this is an example of one specific helicopter (UH-1C), not all helicopters will have all of the parts listed in Figure 2.1.

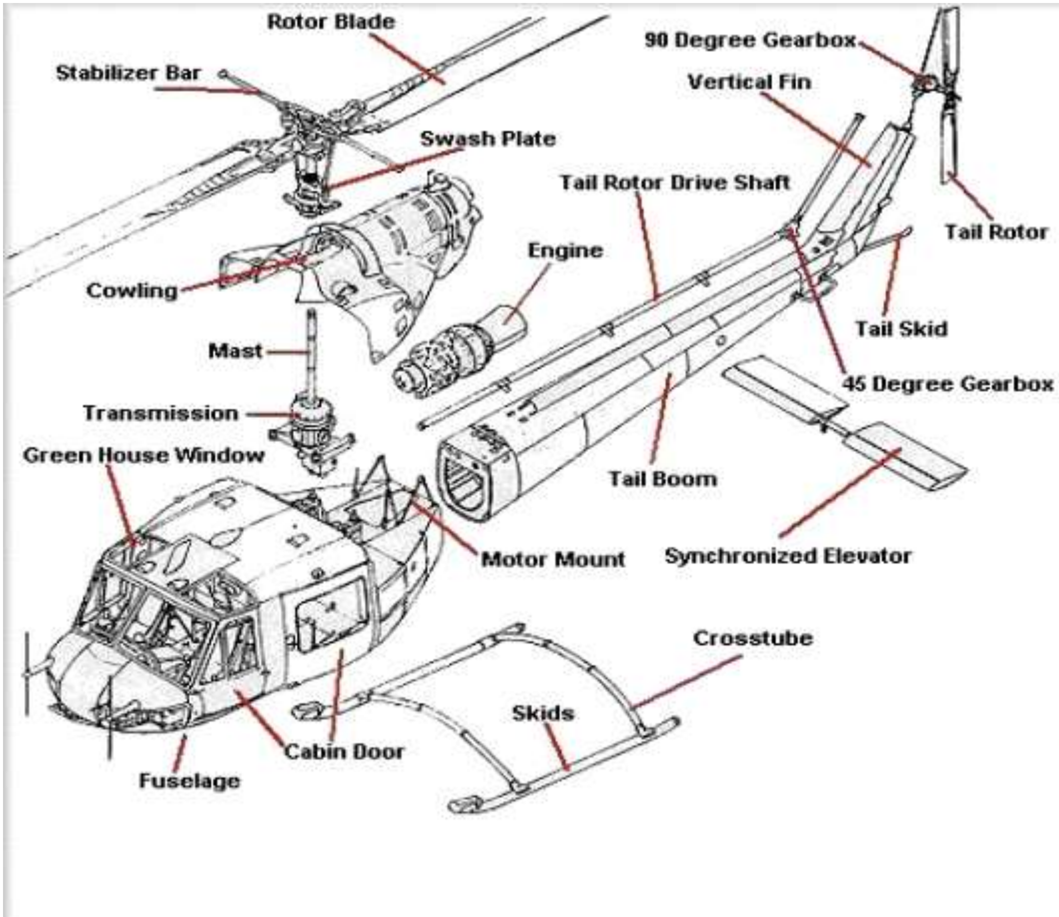

Figure 2.1 Helicopter Configurations [8]

2.1 Main Rotor System

The rotor system of a helicopter is the unit that is composed of a hub and the blades attached to it. Each rotor is considered a separate system, and a helicopter may have more than one main rotor.

Main rotor system generally consists of hub, mast; control tubes pitch change horn, and pitch, nut, blade grips and root. There are three primary types of rotor systems: articulated, semi-rigid, and rigid [9].

The articulated rotor system first appeared on the auto gyros of the 1920s and is the oldest and most widely used type of rotor system. The rotor blades in this type of system can move in three ways as it turns around the rotor hub and each blade can move independently of the others. They can move up and down (flapping), back and forth in the horizontal plane, and can change in the pitch angle (the tilt of the blade) [9].

In the semi-rigid rotor system, the blades are attached rigidly to the hub but the hub itself can tilt in any direction about the top of the mast. This system generally appears on helicopters with two rotor blades. These systems resemble a seesaw when one blade is pushed down, the opposite one rises [9].

The rigid rotor system resembles an ordinary propeller and is the least often used. The blades are fixed to the hub without hinges and the hub is fixed to the shaft. The blades on rigid rotor systems flex. This configuration is most like the airscrew envisioned by Leonardo da Vinci and George Cayley [9].

Root is the inner end of the blade where the rotors connect to the blade grips.

Blade Grips are the large attaching points where the rotor blade connects to the hub.

Hub sits atop the mast, and connects the rotor blades to the control tubes.

Mast is the rotating shaft from the transmission, which connects the rotor blades to the helicopter.

Control Tubes push and pull tubes that change the pitch of the rotor blades.

Pitch Change Horn is the armature that converts control tube movement to blade pitch.

Pitch increased or decreased angle of the rotor blades to rise, lower, or change the direction of the rotors thrust force.

2.2 Tail Rotor System

One of the very first problems helicopter designers encountered when they tried to create a machine that could hover was the problem of torque reaction. Newton's third law of motion requires that for every action there is an equal and opposite action This component of helicopter is the tail rotor. Igor Sikorsky seems to be the first to settle on using a single rotor mounted at the rear of the helicopter as a way to counter the torque [9]. The tail rotor is very important. If you spin a rotor with an engine, the rotor will rotate, but the engine and helicopter body will tend to rotate in opposite direction to the rotor. This is called Torque reaction. Newton's third law of motion states, "To every action there is an equal and opposite reaction". The tail rotor is used to compensate for this torque and hold the helicopter straight. On twin-rotors helicopter, the rotors spin in opposite directions, so their reactions cancel each other. The tail rotor is normally linked to the main rotor via a system of drive shafts and gearboxes, which means if you turn the main rotor; the tail rotor is also turn. Most helicopters have a ratio of 3:1 to 6:1. That is, if main rotor turns one rotation, the tail rotor will turn 3 revolutions (for 3:1) or 6 revolutions (for 6:1) [10]. In most helicopters the engine turns a shaft that connected to an input quill in the transmission gearbox. The main rotor mast is out to the top and tail rotor drive shafts out to the tail from the transmission gear box. Tail rotors rob an enormous amount of power. As a rule of thumb, tail rotors consume up to 30% of the engine power [9].

2.3 Control System

In the early Cierva autogyros, the rotor was simply a lifting device and roll and pitch control were obtained by ailerons on stub wings and by a conventional elevator, neither of which was very effective at low speed. Following years, Cierva developed a means of obtaining direct control by tilting the rotor on gimbals with respect to the shaft [7]. By this way, pitch and roll control were obtained. Cyclic pitch was developed when the control forces required to tilt the rotor became so high that flight was difficult. Cyclic is the left and right, forward and aft control. It puts in one control input into the rotor system at a time through the swash plate. It is also known as the "Stick". It comes out of the center of the floor of the cockpit, and sits between the pilots' legs. It is operated by the pilots' right hand.

In the helicopter control system which is almost universally used at present, the pilot cyclically changes the pitch of the blades about feathering bearings by tilting a mechanism known as a swash plate. It turns non-rotating control movements into rotating control movements.

Collective is the up and down control. It puts a collective control input into the rotor system, meaning that it puts either "all up", or "all down" control inputs in at one time through the swash plate. It is operated by the stick on the left side of the seat, called the collective pitch control. It is operated by the pilots' left hand.

Pedals are not rudder pedals, although they are in the same place as rudder pedals on an airplane. A single rotor helicopter has no real rudder. It has instead, an anti-torque rotor (Also known as a tail rotor), which is responsible for directional control at a hover, and aircraft trim in forward flight. The pedals are operated by the pilots' feet, just like airplane rudder pedals are. Tandem rotor helicopters also have these pedals, but they operate both main rotor systems for directional control at a hover [8].

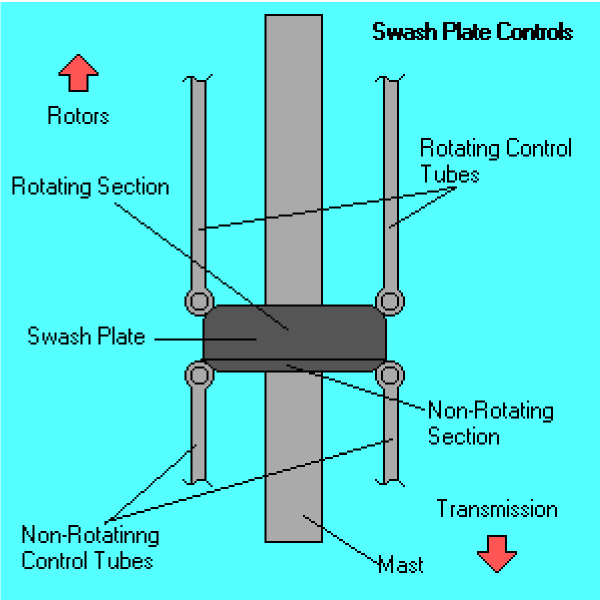

Figure 2.2 Control Systems [8]

A schematic of a control system is shown in Figure 2.2.

3. IMPORTANCE OF AIRFOIL SHAPE AND TIP SHAPE

Main rotor performance can be increased by using advanced single element airfoils and new rotor blade planforms.

The development of rotors will allow larger payload capability, higher forward flight speeds, increased range and endurance, and greater maneuverability and agility [6].

The airfoil shape has a high effect on performance of rotor. There are some criteria's to select an airfoil or airfoils for the optimum helicopter design. The airfoil should satisfy high maximum static and dynamic lift coefficients to allow flight at high tip speed ratios and/or at high maneuver load factors, high drag divergence Mach number to allow flight at advancing tip Mach numbers without prohibitive power loses or noise, low drag at moderate lift coefficients and Mach numbers to minimize the power in normal flight conditions, a low pitching moment to minimize blade torsion moments and control loads, an aft aerodynamic center position to minimize the nose ballast required to balance the blade, enough thickness for efficient structure, and the last one, easy to manufacture contours. However, the studies of airfoil characteristics show that these characteristics do not go together in any one airfoil.

The other factors that influence the rotor performance are the tip shape and planform of rotor. There are varieties of reasons to select different tip shapes instead of the usual square one. Use of leading edge sweep is the most common one to reduce the compressibility effects on the advancing tip at high forward speeds. The jet transport's swept-back wing is an example for this. There are two compressibility effects that have proved to be significant: the generation of high blade torsion and control loads through Mach Tuck and the generation of noise by propagated shock waves. By sweeping the leading edge of the tip, both of these disturbing phenomena can be delayed to forward speeds above the helicopter's normal speed range. Another reason for using special tip shape is to decrease the blade loads and noise produced by each blade moving into a fluid which has already been disturbed by a previous blade. The tip vortex left by a preceding blade could be scattered by using a special tip shape. However, this opinion is reasonable but as yet unverified hypothesis. Swept-back tips have yet another potential advantage: dynamic twist [7]. On the advancing tip at high forward speeds, most of the twisted blades carry a non advantageous downward load. If the tip is swept back, this download acts behind the structural axis and tends to twist the blade nose up, thus reducing the download and its aerodynamic penalty. On the retreating side, the upload on the swept tip twists the blade nose down and alleviates retreating blade stall. This advent can be seen when the helicopter flight on hover position. Figure 3.1 shows various tip shapes, some of which used on contemporary helicopters.

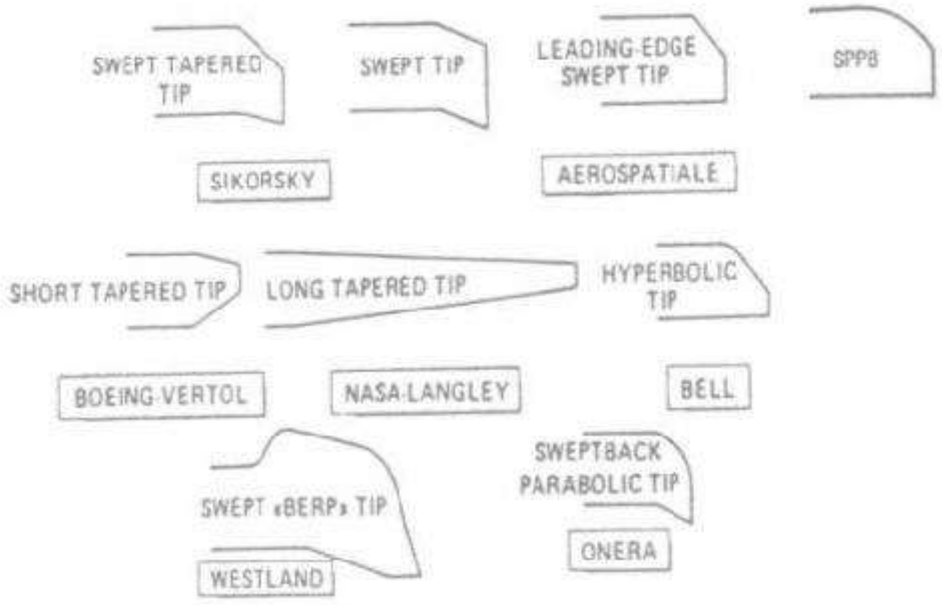

Figure 3.1 Examples of Blade Tips Either Already Produced or Under Development [18]

Another factor that should improve the performance of rotor is the blade taper. Taper blade increase in quality hovering performance by unloading the tips to obtain a more uniform induced velocity through the rotor disc. This improvement achieved by taper blade is used in early helicopters. According to Prouty [7] some factors should be considered before deciding whether to use taper or not. When the taper blade is used in small helicopters, it makes the tip chord small and suffers goals in drag and in maximum lift coefficient weights. Second careful attention is about tip weights. Most rotor blades have tip weights either to improve the autorotational capability or to control dynamic characteristics by placing the frequency of the second blade bending mode below three times per revolution (3/rev) [7]. Moreover, a tapered blade needs more area to generate the same thrust value with straight blade. This modification increases the performance in hover and vertical climb, but it also decreases the payload advantage because of the increased area.

4. MATHEMATICAL AND NUMERICAL FORMULATION OF THE ROTOR PERFORMANCE

4.1 Mathematical Formulation

4.1.1 The Governing Equations

The governing equations for the rotor blade analysis are the Navier-Stokes equations. For inviscid flow considerations the Euler equations are employed. In this case, the mass conservation equation is the same as for viscous flow, but the momentum and energy conservation equations are reduced due to the absence of molecular diffusion. The equations given below are in the form employed by the commercial code Fluent [12].

4.1.1.1 The Mass Conservation Equation

The equation for conservation of mass or continuity equation can be written as follows:

$$\frac{\partial \rho}{\partial t} + \nabla.(\rho \vec{\upsilon}) = S_m \tag{4.1}$$

Equation (4.6) is the general form of the mass conservation equation and is valid for incompressible as well as compressible flows. The source S_m is the mass added to the continuous phase from the dispersed second phase (e.g., due to vaporization of liquid droplets) and any user-defined sources.

4.1.1.2 Momentum Conservation Equations

Conservation of momentum is described by

$$\frac{\partial}{\partial t}(\rho \vec{\upsilon}) + \nabla.(\rho \vec{\upsilon}\vec{\upsilon}) = -\nabla p + \rho \vec{g} + \vec{F} \tag{4.2}$$

Where p is the static pressure, $\rho \vec{g}$ and $\vec{F}$ are the gravitational body force and external body forces (e.g., forces that arise from interaction with the dispersed phase), respectively. F also contains other model-dependent source terms such as porous- media and user-defined sources.

4.1.1.3 Energy Conservation Equation

Conservation of energy is described by

$$\frac{\partial}{\partial t}(\rho E)+\nabla.(\vec{\upsilon}(\rho E+p))=-\nabla.\left(\sum_j h_j J_j\right) \tag{4.3}$$

J is the diffusion flux and sensible enthalpy h is defined for ideal gases.

4.2 Rotating Reference Frame

When a model is created using Fluent, the user is typically modeling the flow in an inertial reference frame (in a non-accelerating coordinate system). However, Fluent also has the ability to model flows in an accelerating reference frame. In this situation, the acceleration of the coordinate system is included in the equations of motion describing the flow. A common example of an accelerating reference frame in engineering applications is flow in rotating equipment. Many such flows can be modeled in a coordinate system that is moving with the rotating equipment and thus experiences a constant acceleration in the radial direction. This class of rotating flows can be treated using the rotating reference frame capability in Fluent.

When such problems are defined in a rotating reference frame, the rotating boundaries become stationary relative to the rotating frame, since they are moving at the same speed as the reference frame.

4.2.1 Equations for a Rotating Reference Frame

When the equations of motion are solved in a rotating frame of reference, the acceleration of the fluid is augmented by additional terms that appear in the Momentum Equations (4.8). Fluent allows you to solve rotating frame problems using either the absolute velocity, $\vec{\upsilon}$ or the relative velocity, $\vec{\upsilon}_r$ as the dependent variable. The two velocities are related by the following equation:

$$\vec{\upsilon}_r=\vec{\upsilon}-\left(\vec{\Omega}*\vec{r}\right) \tag{4.4}$$

Here, $\vec{\Omega}$ is the angular velocity vector (that is, the angular velocity of the rotating frame) and $\vec{r}$ is the position vector in the rotating frame.

The left-hand side of the momentum Equation (4.2) appears as follows for an inertial reference frame:

$$\frac{\partial}{\partial t}(\rho\vec{v})+\nabla.(\rho\vec{v}\vec{v}) \tag{4.5}$$

For a rotating reference frame, the left-hand side written in terms of absolute velocities becomes

$$\frac{\partial}{\partial t}(\rho\vec{v})+\nabla.(\rho\vec{v}_r\vec{v})+\rho\left(\vec{\Omega}x\vec{v}\right) \tag{4.6}$$

In terms of relative velocities the left-hand side is given by

$$\frac{\partial}{\partial t}(\rho\vec{v}_r)+\nabla.(\rho\vec{v}_r\vec{v}_r)+\rho\left(2\vec{\Omega}x\vec{v}_r+\vec{\Omega}x\vec{\Omega}x\vec{r}\right)+\rho\frac{\partial\vec{\Omega}}{\partial t}x\vec{r} \tag{4.7}$$

where $\rho(2\vec{\Omega}x\vec{v}_r)$ is the Coriolis force. Note that Fluent neglects the $\rho\frac{\partial\vec{\Omega}}{\partial t}x\vec{r}$ term, so it cannot accurately model a time-varying angular velocity using the relative velocity formulation.

For flows in rotating domains, the equation for conservation of mass, or continuity equation, can be written for both the absolute and the relative velocity formulations.

4.3 Turbulence Modeling

4.3.1 Spalart-Allmaras Model

In turbulence models that employ the Boussinesq approach, the central issue is how the eddy viscosity is computed. The model proposed by Spalart and Allmaras solves a transport equation for a quantity that is a modified form of the turbulent kinematic viscosity.

4.3.1.1 Transport Equation for the Spalart-Allmaras Model

The transported variable in the Spalart-Allmaras model, $\tilde{\nu}$, is identical to the turbulent kinematics viscosity except in the near-wall (viscous-affected) region. The transport equation for $\tilde{\nu}$ is;

$$\frac{\partial}{\partial t}(\rho\tilde{\upsilon})+\frac{\partial}{\partial x_i}(\rho\tilde{\upsilon}u_i)$$
$$=G_\upsilon+\frac{1}{\sigma_{\tilde{\upsilon}}}\left[\frac{\partial}{\partial x_j}\left\{(\mu+\rho\tilde{\upsilon})\frac{\partial\tilde{\upsilon}}{\partial x_j}\right\}+Cb2\rho\left(\frac{\partial\tilde{\upsilon}}{\partial x_j}\right)^2\right]-Y_v+S_{\tilde{\upsilon}} \tag{4.8}$$

Since the turbulence kinetic energy k is not calculated in the Spalart-Allmaras model, the last term in Equation (4.13) is ignored when estimating the Reynolds stresses.

4.3.1.2 Modeling the Turbulent Viscosity

The turbulent viscosity, μ_t, is computed from

$$\mu_t = \rho\tilde{\upsilon}f_{\upsilon 1} \tag{4.9}$$

Where the viscous damping function, f_{v1}, is given by

$$f_{\upsilon 1} = \frac{X^3}{X^3 + C_{\upsilon 1}^3} \tag{4.10}$$

and

$$X \equiv \frac{\tilde{\upsilon}}{\upsilon} \tag{4.11}$$

4.3.1.3 Modeling the Turbulent Production

The production term, G_v, is modeled as

$$G_\upsilon = C_{b1}\rho\tilde{S}\tilde{\upsilon} \tag{4.12}$$

where

$$\tilde{S} \equiv S + \frac{\tilde{\upsilon}}{k^2 d^2} f_{v2} \tag{4.13}$$

and

$$f_{\upsilon 2} = 1 - \frac{X}{1 + Xf_{\upsilon 1}} \tag{4.14}$$

By default in Fluent, as in the original model proposed by Spalart and Allmaras, S is based on the magnitude of the vorticity;

$$S \equiv \sqrt{2\Omega_{ij}\Omega_{ij}} \tag{4.15}$$

where Ω_{ij} is the mean rate-of-rotation tensor and is defined by

$$\Omega_{ij} = \frac{1}{2}\left(\frac{\partial u_i}{\partial x_j} - \frac{\partial u_j}{\partial x_i}\right) \tag{4.16}$$

The justification for the default expression for S is that, for the wall-bounded flows that were of most interest when the model was formulated, turbulence is found only where vorticity is generated near walls. However, it has since been acknowledged that one should also take into account the effect of mean strain on the turbulence production, and a modification to the model has been proposed and incorporated into Fluent. This modification combines measures of both rotation and strain tensors in the definition of S;

$$S \equiv \left|\Omega_{ij}\right| + C_{prod}\min\left(0, \left|S_{ij}\right| - \left|\Omega_{ij}\right|\right) \tag{4.17}$$

where

$$C_{prod} = 2, \quad \left|\Omega_{ij}\right| \equiv \sqrt{2\Omega_{ij}\Omega_{ij}}\ , \quad \left|S_{ij}\right| \equiv \sqrt{2S_{ij}S_{ij}} \tag{4.18}$$

with the mean strain rate, S_{ij}, defined as

$$S_{ij} = \frac{1}{2}\left(\frac{\partial u_j}{\partial x_i} + \frac{\partial u_i}{\partial x_j}\right) \tag{4.19}$$

Including both the rotation and strain tensors reduces the production of eddy viscosity and consequently reduces the eddy viscosity itself in regions where the measure of vorticity exceeds that of strain rate. One such example can be found in vortical flows, i.e., flow near the core of a vortex subjected to a pure rotation where turbulence is known to be suppressed. Including both the rotation and strain tensors more correctly accounts for the effects of rotation on turbulence. The default option (including the rotation tensor only) tends to over predict the production of eddy viscosity and hence over predicts the eddy viscosity itself in certain circumstances.

4.3.2 The Standard k-ε Model

The standard $k-\varepsilon$ model is a semi-empirical model based on model transport equations for the turbulence kinetic energy (k) and its dissipation rate (ε). The model transport equation for k is derived from the exact equation, while the model transport equation for ε was obtained using physical reasoning and bears little resemblance to its mathematically exact counterpart. The simplest “complete models" of turbulence are two-equation models in which the solution of two separate transport equations allows the turbulent velocity and length scales to be independently determined. Robustness, economy, and reasonable accuracy for a wide range of turbulent flows explain its popularity in industrial flow and heat transfer simulations. It is a semi-empirical model, and the derivation of the model equations relies on phenomenological considerations and empiricism.

4.3.2.1 Transport Equations for the Standard k-ε Model

The turbulence kinetic energy, k, and its rate of dissipation, ε, are obtained from the following transport equations:

$$\frac{\partial}{\partial t}(\rho k)+\frac{\partial}{\partial x_i}(\rho k u_i) = \frac{\partial}{\partial x_j}\left[\left(\mu+\frac{\mu_t}{\sigma_k}\right)\frac{\partial k}{\partial x_j}\right]+G_k+G_b-\rho\varepsilon-Y_M+S_k \tag{4.20}$$

and

$$\frac{\partial}{\partial t}(\rho\varepsilon)+\frac{\partial}{\partial x_i}(\rho\varepsilon u_i) = \frac{\partial}{\partial x_j}\left[\left(\mu+\frac{\mu_t}{\sigma_\varepsilon}\right)\frac{\partial\varepsilon}{\partial x_j}\right]+C_{1\varepsilon}\frac{\varepsilon}{k}\left(G_k+C_{3\varepsilon}G_b\right)-C_{2\varepsilon}\upsilon\frac{\varepsilon^2}{k}+S_\varepsilon \tag{4.21}$$

In these equations, G_k represents the generation of turbulence kinetic energy due to the mean velocity gradients.

G_b is the generation of turbulence kinetic energy due to buoyancy,

Y_M represents the contribution of the fluctuating dilatation in compressible turbulence to the overall dissipation rate.

$C_{1\varepsilon}$, $C_{2\varepsilon}$, and $C_{3\varepsilon}$ are constants.

σ_k and σ_ε are the turbulent Prandtl numbers for k and ε, respectively.

S_k and S_ε are user-defined source terms.

4.3.2.2 Modeling the Turbulent Viscosity

The turbulent (or eddy) viscosity, μ_t, is computed by combining k and ε as follows:

$$\mu_t = \rho C_\mu \frac{k^2}{\varepsilon} \tag{4.22}$$

C_μ is a constant.

4.4 Numerical Method

In Fluent, two numerical solution methods, segregated and coupled solver, are allowed user to choose in the solution procedure. Using either method, Fluent will solve the governing integral equations for the conservation of mass and momentum, and (when appropriate) for energy and other scalars such as turbulence and chemical species. In both cases a control-volume-based technique is used that consists of division of the domain into discrete control volumes using a computational grid, integration of the governing equations on the individual control volumes to construct algebraic equations for the discrete dependent variables (``unknowns'') such as velocities, pressure, temperature, and conserved scalars, linearization of the discretized equations and solution of the resultant linear equation system to yield updated values of the dependent variables.

The two numerical methods employ a similar discretization process (finite-volume), but the approach used to linearize and solve the discretized equations is different.

4.4.1 Segregated Solution Method

The segregated solver is the solution algorithm used by Fluent. Using this approach, the governing equations are solved sequentially (segregated from one another). Because the governing equations are non-linear (and coupled), several iterations of the solution loop must be performed before a converged solution is obtained. Each iteration consists of the steps outlined below:

- Fluid properties are updated, based on the current solution. (If the calculation has just begun, the fluid properties will be updated based on the initialized solution.)
- The u, v, and w momentum equations are each solved in turn using current values for pressure and face mass fluxes, in order to update the velocity field.

- Since the velocities obtained in Step 2 may not satisfy the continuity equation locally, a "Poisson-type" equation for the pressure correction is derived from the continuity equation and the linearized momentum equations. This pressure correction equation is then solved to obtain the necessary corrections to the pressure and velocity fields and the face mass fluxes such that continuity is satisfied.
- Where appropriate, equations for scalars such as turbulence, energy, species, and radiation are solved using the previously updated values of the other variables.
- When interphase coupling is to be included, the source terms in the appropriate continuous phase equations may be updated with a discrete phase trajectory calculation.
- A check for convergence of the equation set is made.

These steps are continued until the convergence criteria are met.

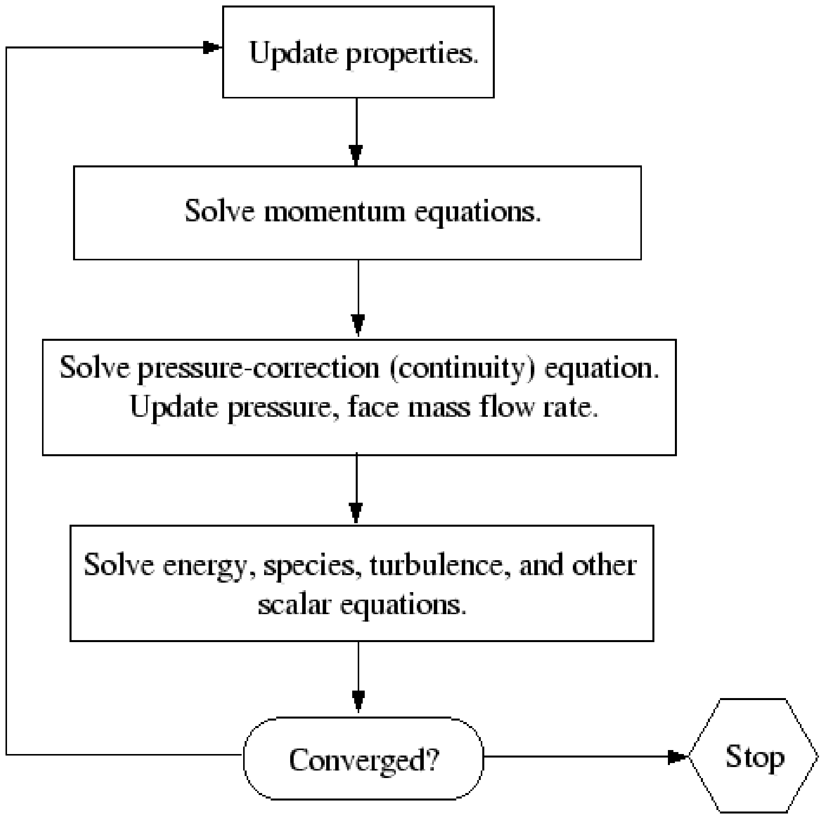

Figure 4.1 Overview of the Segregated Solution Method

4.4.2 Coupled Solution Method

The coupled solver solves the governing equations of continuity, momentum, and (where appropriate) energy and species transport simultaneously (coupled together). Governing equations for additional scalars will be solved sequentially (segregated from one another and from the coupled set) using the procedure described for the segregated solver in the previous section. Because the governing equations are non-linear (and coupled), several iterations of the solution loop must be performed before a converged solution is obtained. Each iteration consists of the outlined below;

- Fluid properties are updated, based on the current solution. (If the calculation has just begun, the fluid properties will be updated based on the initialized solution.)
- The continuity, momentum, and (where appropriate) energy and species equations are solved simultaneously.
- Where appropriate, equations for scalars such as turbulence and radiation are solved using the previously updated values of the other variables.
- When interphase coupling is to be included, the source terms in the appropriate continuous phase equations may be updated with a discrete phase trajectory calculation.
- A check for convergence of the equation set is made.

These steps are continued until the convergence criteria are met.

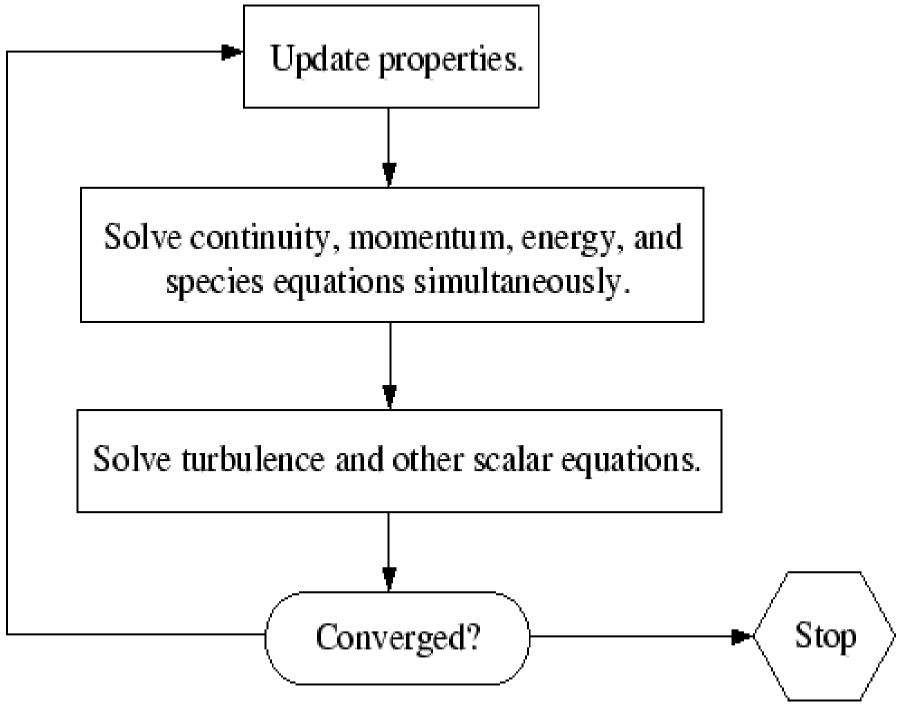

Figure 4.2 Overview of the Coupled Solution Method

4.4.3 Linearization

In both the segregated and coupled solution methods the discrete, non-linear governing equations are linearized to produce a system of equations for the dependent variables in every computational cell. The resultant linear system is then solved to yield an updated flow-field solution.

The manner in which the governing equations are linearized may take an "implicit" or "explicit" form with respect to the dependent variable (or set of variables) of interest.

4.4.3.1 Explicit Scheme of Analysis

For a given variable, the unknown value in each cell is computed using a relation that includes only existing values. Therefore, each unknown will appear in only one equation in the system and the equations for the unknown value in each cell can be solved one at a time to give the unknown quantities.

In the segregated solution method each discrete governing equation is linearized implicitly with respect to that equation's dependent variable. This will result in a system of linear equations with one equation for each cell in the domain. Because there is only one equation per cell, this is sometimes called a "scalar" system of equations. A point implicit (Gauss-Seidel) linear equation solver is used in conjunction with an algebraic multigrid (AMG) method to solve the resultant scalar system of equations for the dependent variable in each cell. For example, the x-momentum equation is linearized to produce a system of equations in which u-velocity is the unknown. Simultaneous solution of this equation system (using the scalar AMG solver) yields an updated u-velocity field.

In summary, the segregated approach solves for a single variable field by considering all cells at the same time. It then solves for the next variable field by again considering all cells at the same time, and so on. There is no explicit option for the segregated solver.

In the coupled solution method the user has a choice of using either an implicit or explicit linearization of the governing equations. This choice applies only to the coupled set of governing equations. Governing equations for additional scalars that are solved segregated from the coupled set, such as for turbulence, radiation, etc., are linearized and solved implicitly using the same procedures as in the segregated solution method. Regardless of whether he/she chooses the implicit or explicit scheme, the solution procedure shown in Figure 4.3 is followed.

4.4.3.2 Implicit Scheme of Analysis

If the user chooses the implicit option of the coupled solver, each equation in the coupled set of governing equations is linearized implicitly with respect to all dependent variables in the set. This will result in a system of linear equations with N equations for each cell in the domain, where N is the number of coupled equations in the set. Because there are N equations per cell, this is sometimes called a ``block'' system of equations. A point implicit (block Gauss-Seidel) linear equation solver is used in conjunction with an algebraic multigrid (AMG) method to solve the resultant block system of equations for all N dependent variables in each cell. In summary, the coupled implicit approach solves for all variables (u, v, w, T) in all cells at the same time.

If the user chooses the explicit option of the coupled solver, each equation in the coupled set of governing equations is linearized explicitly. As in the implicit option, this too will result in a system of equations with N equations for each cell in the domain. And likewise, all dependent variables in the set will be updated at once. In summary, the coupled explicit approach solves for all variables (p, u, v, w, T) one cell at a time.

4.4.4 Discretization of Equations

Fluent uses a control-volume-based technique to convert the governing equations to algebraic equations that can be solved numerically. This control volume technique consists of integrating the governing equations about each control volume, yielding discrete equations that conserve each quantity on a control-volume basis.

Discretization of the governing equations can be illustrated most easily by considering the steady-state conservation equation for transport of a scalar quantity Φ. This is demonstrated by the following equation written in integral form for an arbitrary control volume V as follows:

$$\oint \rho\phi\vec{v}.d\vec{A} = \oint \Gamma_\phi \nabla\phi.dA + \int S_\phi dV \qquad (4.23)$$

Equation (4.32) is applied to each control volume, or cell, in the computational domain. The two-dimensional, triangular cell shown in Figure 4.3 is an example of such a control volume. Discretization of Equation (4.32) on a given cell yields

$$\sum_f^{N_{faces}} \rho f\vec{v}_f \phi_f .\vec{A}_f = \sum_f^{N_{faces}} \Gamma_\phi (\nabla\phi)_n .\vec{A}_f + S_\phi V \qquad (4.24)$$

The equations solved by Fluent take the same general form as the one given above and apply readily to multi-dimensional, unstructured meshes composed of arbitrary polyhedral.

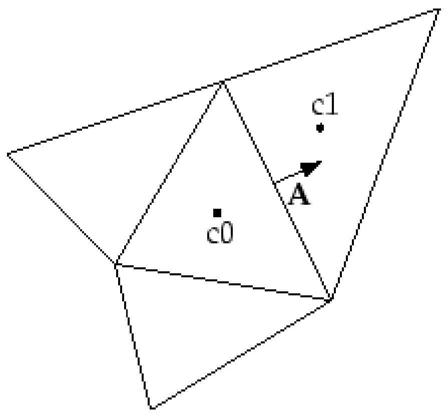

Figure 4.3 Control Volume Used to Illustrate Discretization of a Scalar Transport Equation

By default, Fluent stores discrete values of the scalar Φ at the cell centers (c_0 and c_1 in Figure 4.3). However, face values Φ_f is required for the convection terms in Equation (4.28) and must be interpolated from the cell center values. This is accomplished using an upwind scheme.

Upwinding means that the face value Φ_f is derived from quantities in the cell upstream or "upwind" relative to the direction of the normal velocity v_n in Equation (4.29). Fluent allows you to choose from several upwind schemes: first-order upwind, second-order upwind, power law, and QUICK.

4.5 Boundary Conditions

4.5.1 Far Field Boundary Conditions

Weakly enforced boundary conditions are employed for all of the calculations. By weak enforcement, we mean that that the boundary conditions are specified in an integral sense over the boundary faces. Strong enforcement requires that each node satisfy the boundary condition exactly [11].

Determination of appropriate boundary conditions which are superposed are very important to obtain realist behavior in the wake of a hovering rotor. In a rotor in forward flight, the rotor wake is rapidly swept away from the rotor and out of the computational domain, in hover position, the wake system remains close to the rotor blades for a number of rotor revolutions. Because of this reason, in hover, definition of appropriate far-field boundary conditions is much more important.

The method described by Srinivasan et al [11] is used to determine inflow/outflow boundary conditions for the hovering rotor. In this method, 1-D helicopter momentum theory is used to approximate the boundary conditions. Momentum theory concerns itself with the global balance of mass, momentum, and energy. It does not concern itself with details of the flow around the blades. It gives a good representation of what is happening far away from the rotor. Momentum Theory has some assumptions about rotor and flowfield. Rotor is modeled as an actuator disk, which adds momentum and energy to the flow. Flow is incompressible, steady, inviscid, irrotational, one-dimensional, uniform through the rotor disk, and also there is no swirl in the far wake.

By using this theory, the far field outflow velocity due to the rotor wake system can be related to the thrust from the rotor blade by

$$W_e = -2M_t\sqrt{\frac{C_t}{2}} \qquad (4.25)$$

This velocity is uniform and occurs below the rotor blade over an exit area equal to one half of the area of the rotor disk which can be seen in Figure 4.4.

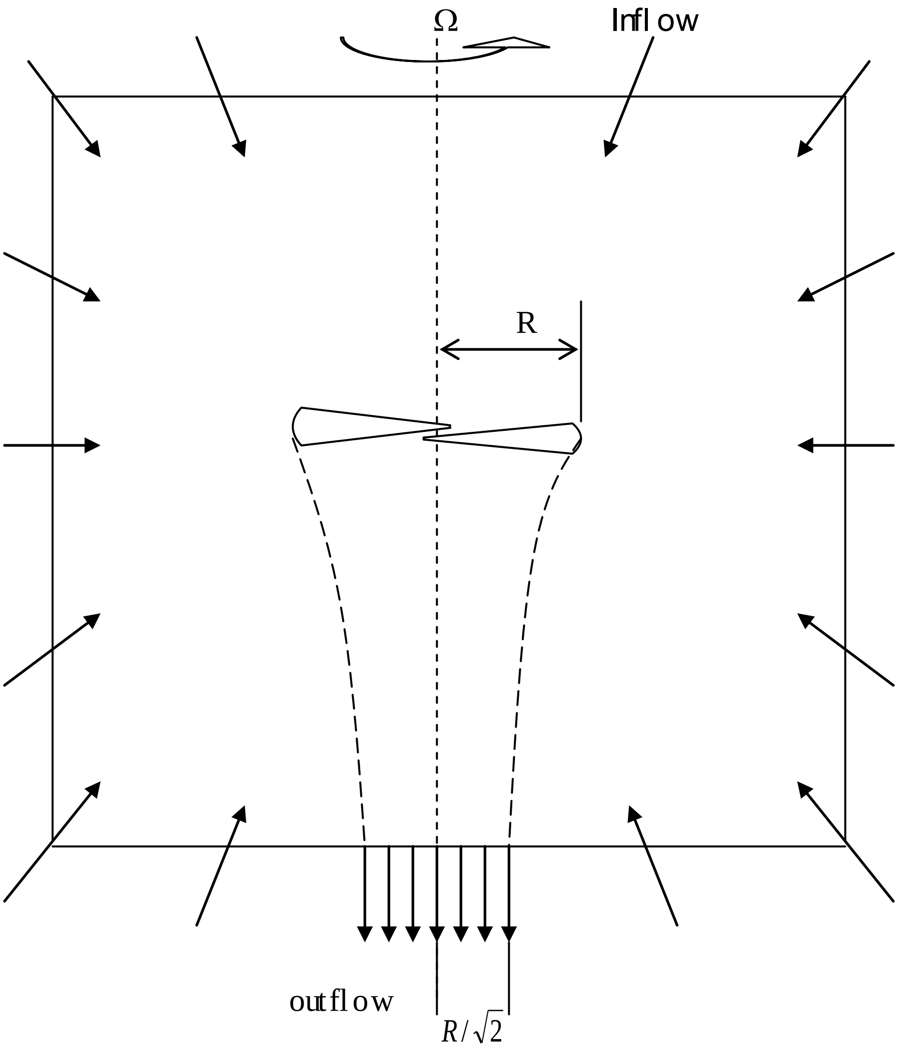

Figure 4.4 Boundary Conditions for the Hovering Rotor [11]

However, values and assumptions made for Momentum Theory are not valid for flow field around rotor. They are used to give suitable far field boundary conditions in the wake of a hovering rotor. Momentum Theory assumptions are combined with the solution around the three dimensional helicopter rotor blades. The flowfield around the blades can be assumed inviscid and steady in hover flight.

In this approach, the rotor is viewed from the far field as a point sink of mass. This results in an inflow at all boundaries equal to

$$W_r = -\frac{M_t}{4}\sqrt{\frac{C_t}{2}}\left(\frac{R}{r}\right)^2 \tag{4.26}$$

This velocity is pointed toward the hub of the rotor blade at all boundary locations [11]. It is illustrated in Figure 4.5.

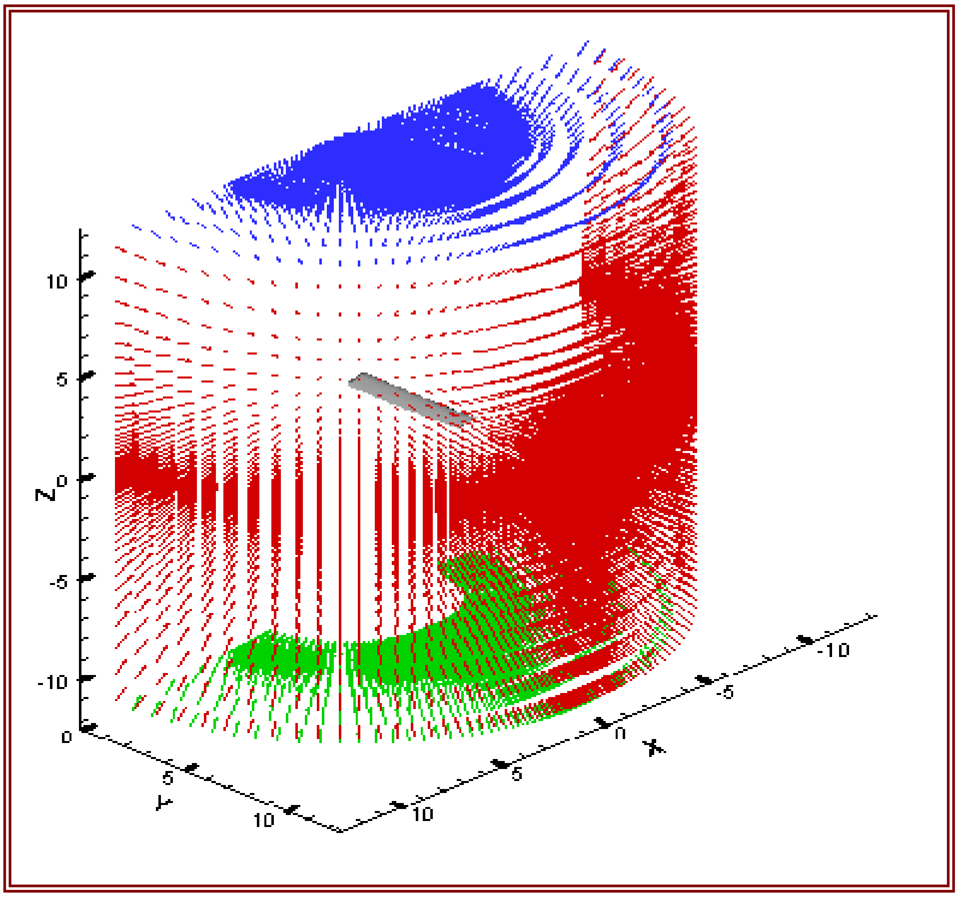

Figure 4.5 Flow Area of Rotor

These inflow/outflow boundary conditions are imposed by a user-defined function (UDF), UDF is a function that you program that can be dynamically loaded with the FLUENT solver to enhance the standard features of the code. UDFs are written in the C programming language. They are defined using DEFINE macros that are supplied by Fluent Inc. They access data from the FLUENT solver using predefined macros and functions also supplied by Fluent Inc [12]. UDF which is used in this work is given in the appendix A.

4.6 Rotorcraft Performance Equations

Following expressions are used to calculate the rotor performance parameters.

$$C_T = \frac{T}{\rho(\pi R^2)(\Omega R)^2} \tag{4.27}$$

$$M_{tip} = \frac{\Omega R}{a_\infty} \tag{4.28}$$

$$C_p = \frac{p - p_\infty}{\frac{1}{2}\rho V^2} \tag{4.29}$$

Where C_T is the thrust coefficient, R is the rotor radius, Ω is the rotor radial speed, Q is the power, p is the static pressure, a is the speed of sound, ρ is the density of air and V is the velocity magnitude, Cp is the pressure coefficient.

5. GRID INFORMATION AND BLADE CONFIGURATIONS

Three-dimensional flow fields around helicopter rotor blades are investigated in hover. The properties of the blade configurations are given in Table 5.1. The two blades, which are investigated in hover position have untwisted, rectangular plan form with an aspect ratio of 6.

The reference rotor is a model two-bladed rotor which has been extensively experimentally and numerically investigated, is called Caradonna-Tung's blade shown in Figure 5.1 consists of NACA0012 and the other one consists of VR7 airfoil, Figure 5.2. They are analyzed in two different tip Mach numbers of 0.439 and 0.877 for collective pitch angles of 0 and 8 degrees. The grids for these configurations are generated using an in-house grid generator developed at Georgia Institute of Technology, Scholl of Aerospace Engineering. It generates a 3-D H-H-O grid primarily used for helicopter rotors. Presently an algebraic H-H grid is first specified. The elliptic equations are then solved in two sweeps; one sweep for each plane in the radial direction then another sweep for each plane in the chord wise direction. This fully 3-D elliptic H-H grid is then wrapped into an O-grid for each azimuthal plane. The axis system used is z vertical, y span wise (from root to tip) and x is axial which forms an orthogonal system. The mesh used in the computations is a 3-D H-H mesh of 131 (chord) x 43 (span) x 61 (vertical). The flowfield consists of 655200 hexahedral cells and 682492 nodes. This grid is shown in Figure 5.3.

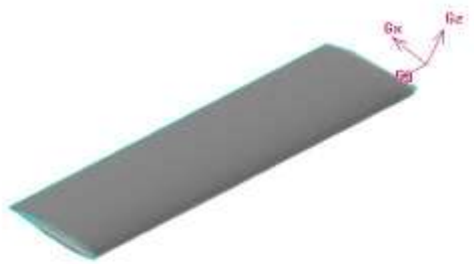

Figure 5.1 Caradonna-Tung's blade

Figure 5.2 Blade with Single VR7 Profile

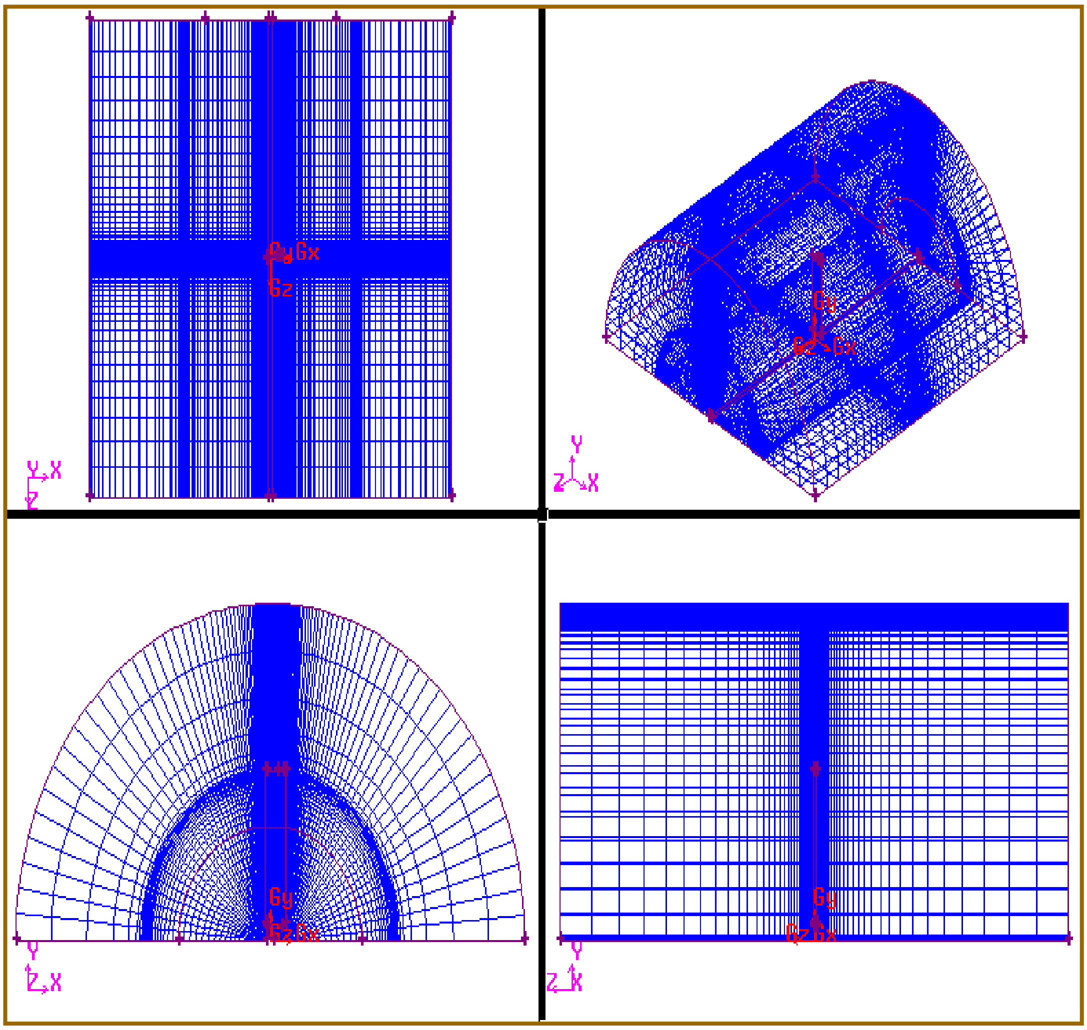

Figure 5.3 Structured Mesh about Caradonna &Tung's blade.

Structured grids shown in Figure 5.3 were produced using in house available software for the analysis. This structured mesh was used to examine Caradonna-Tung's blade with NACA0012 and the other one with VR7 airfoil.

Table. 5.1 Blade Configurations

	Square (Caradonna-Tung's[4])	Square (Generic)	Tapered (Martin and Leishman [19])	Swept (Martin and Leishman [19])	Square (Martin and Leishman [19]))
Radius, R	198 mm	198 mm	410 mm	407.99 mm	406 mm
Chord, c	33 mm	33 mm	44 mm	44 mm	44.5 mm
Root cutout, r_o	0.6c	0.6c	0.2R	0.2R	0.2R
Tip speed, ΩR	143 and 289 m/s	143 and 289 m/s	91.32 m/s	89.72 m/s	89.28 m/s
Airfoil section	NACA 0012	VR7	NACA 2415	NACA 2415	NACA 2415
Collective pitch	8^0	8^0	6^0	4.5^0	4.5^0
Twist, Θ_{tw}	0^0	0^0	0^0	0^0	0^0
Tip Mach Number, M_{tip}	0.439 and 0.877	0.439 and 0.877	0.3	0.3	0.26
Thrust coefficients, C_T	0.004565	-	0.00259	0.00258	0.0022
Solidity	0.1	0.1	0.029	0.034	0.035
Tip Chord, c_t	33 mm	33 mm	17.6 mm	44 mm	44.5 mm
Root Chord	33 mm	33 mm	44 mm	44 mm	44.5 mm
Taper ratio, τ	-	-	0.4	-	-
Break point, r_b	-	-	0.8 R	0.8 R	-

The blade parameters of Caradonna &Tung's, Generic with VR7 profile and Leishman &Martin included square, swept and tapered tip configurations are given in Table 5.1.

Finally, the study of tip shape effects on rotor performance is performed. For this study, three different blade geometries with different blade tip shapes including square, tapered, and swept are used. The blade geometries were drawn by using CATIA V5R12 program and their computational domains were generated by Gridgen grid generation software. Tapered tip blade with constant airfoil NACA2415 is seen in Figure 5.4. The blade with swept tip is shown in Figure 5.5.

Figure 5.4 Tapered Tip Blade

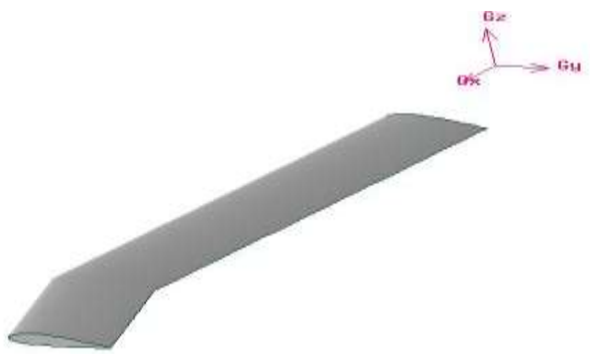

Figure 5.5 Swept Tip Blade

Gridgen [21] is a software system for the generation of three-dimensional grids and meshes. Structured grids consisting entirely of hexahedral cells was used near the rotor blade and for the remaining parts of the computational domain unstructured grids composed of tetrahedral, pyramid, and prism cells having no implicit order was preferred. The overall grid was hybrid, since the grid consisted of both structured and unstructured parts. When the structured grid near the rotor blade was generated, y^+ values were taken so that they are suitable for the viscous solution using The Standard k-ε turbulence model. For best results with Standard k-ε turbulence model, Fluent advise to the user to use either a very fine near-wall mesh spacing on the order of $y^+ = 1$ or a mesh spacing such that $y^+ \geq 30$. Especially, y^+ values near the tip of blade are very effective on the results of the different tip shaped blades. The hybrid grid for the swept tip blade with NACA2415 airfoil is shown in Figure 5.6.

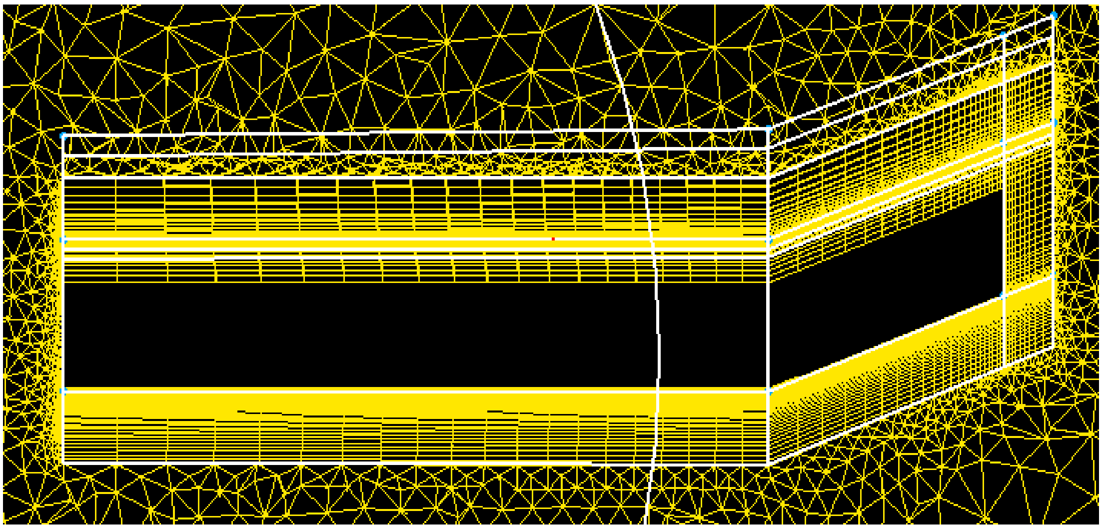

Figure 5.6 Hybrid Grid for the Swept Tip Blade

At the beginning of the analysis, appropriate rotational velocity was given to the flow field for different M_{tip} values.

The grid properties for all the cases considered are given in Table 5.2.

Table 5.2 Grid Properties

Tip Shape	Profile	Collective Pitch angle	M_{tip}	Cell #	Node #
Square	VR7	0^0	0.877	655200 hexahedral	682492
Square	VR7	0^0	0.439	655200 hexahedral	682492
Square	VR7	8^0	0.439	655200 hexahedral	682492
Square	VR7	8^0	0.877	655200 hexahedral	682492
Square	NACA0012	8^0	0.877	655200 hexahedral	682492
Square	NACA0012	8^0	0.439	655200 hexahedral	682492
Square	NACA2415	4.5^0	0.260	648624 mixed	312301
Tapered	NACA2415	6^0	0.300	977427 mixed	270200
Swept	NACA2415	4.5^0	0.300	665997 Mixed	252951

Table 5.2 shows the number of cells and nodes of the meshes used in the analysis of helicopter rotor blades.

6. IMPLEMENTATION OF INITIAL AND BOUNDARY CONDITIONS

Various boundary conditions are employed to carry out the flow analysis. For far field boundary conditions, the equations obtained from 1-D blade element theory were utilized. Velocity inlet boundary condition was used. A user defined function (UDF) was applied to give the values of the inlet velocities at the boundary faces. For outflow, pressure outlet was used. This outflow boundary condition needs to specify the static pressure, temperature, and the direction of the flow.

Periodic boundary conditions are used in solver. For N bladed hovering rotor calculations only one blade, and 1/N of the cylindrical domain need to be considered. Then, the up and downstream boundary planes can be treated as periodic boundaries [5]. All the boundary conditions applied are shown in Figure 6.1.

Moving reference frame was chosen for fluid type, and the appropriate rotational velocity was given for different M_{tip} values.

The ideal gas law was chosen to define the density. Operating pressure is significant for incompressible ideal gas flows because it directly determines the density [12]. Operating pressure was taken 101325 Pa. Therefore, the energy equation was activated to utilize the ideal gas law.

6.1 Periodicity

Periodic boundary conditions are used when the physical geometry of interest and the expected pattern of the flow solution have a periodically repeating nature. Rotationally periodic boundary that forms an included angle about the centerline of a rotationally symmetric geometry is used [12].

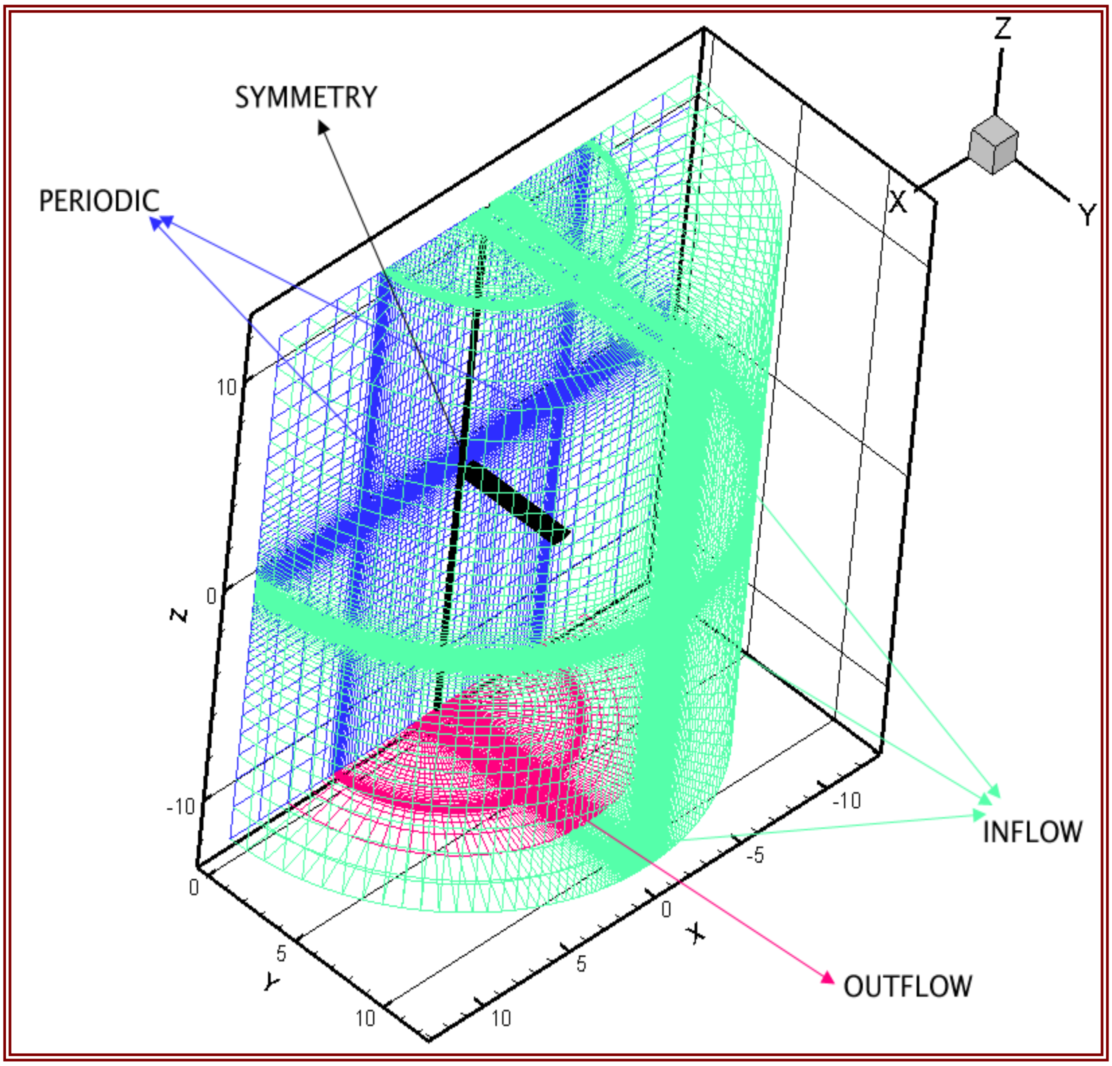

Figure 6.1 Computational Domain

6.2 Velocity Inlet Boundary Conditions

Velocity inlet boundary conditions are used to define the flow velocity, along with all relevant scalar properties of the flow, at flow inlets. The total (stagnation) properties of the flow are not fixed, so they will rise to whatever value is necessary to provide the prescribed velocity distribution.

The boundary condition inputs at velocity inlets are used to compute the mass flow into the domain through the inlet and to compute the fluxes of momentum, energy, and species through the inlet.

When the velocity inlet boundary condition defines flow entering the physical domain of the model, Fluent uses both the velocity components and the scalar quantities that user defined as boundary conditions to compute the inlet mass flow rate, momentum fluxes, and fluxes of energy and chemical species. The mass flow rate entering a fluid cell adjacent to a velocity inlet boundary is computed as

$$\dot{m} = \int \rho \vec{\upsilon} . d\vec{A} \tag{6.1}$$

Only the velocity component normal to the control volume face contributes to the inlet mass flowrate.

Sometimes a velocity inlet boundary is used where flow exits the physical domain. This approach might be used, for example, when the flowrate through one exit of the domain is known or is to be imposed on the model. In such cases user must ensure that overall continuity is maintained in the domain.

In the segregated solver, when flow exits the domain through a velocity inlet boundary Fluent uses the boundary condition value for the velocity component normal to the exit flow area. It does not use any other boundary conditions that you have input. Instead, all flow conditions except the normal velocity component are assumed to be those of the upstream cell.

In the coupled solvers, if the flow exits the domain at any face on the boundary, that face will be treated as a pressure outlet with the pressure prescribed in the Outflow Gauge Pressure field.

6.3 Pressure Outlet Boundary Conditions

Pressure outlet boundary conditions require the specification of a static (gauge) pressure at the outlet boundary. The value of static pressure specified is used only while the flow is subsonic. Should the flow become locally supersonic, the specified pressure is no longer used; pressure will be extrapolated from the flow in the interior. All other flow quantities are extrapolated from the interior.

A set of “backflow” conditions is also specified to be used if the flow reverses direction at the pressure outlet boundary during the solution process. Convergence difficulties will be minimized if you specify realistic values for the backflow quantities.

The program also provides an option to use a radial equilibrium outlet boundary condition and an option to specify a target mass flowrate for pressure outlets.

6.4 Symmetry Boundary Conditions

When the physical geometry of interest, and the expected pattern of the flow solution have mirror symmetry, this boundary condition is used [12]. By using symmetry boundary condition, user can model zero-shear slip walls in viscous flows. It was used for the grid which is generated using an in-house grid generator developed at Georgia Institute of Technology. The grid with symmetry boundary condition can be seen in Figure 6.1. The hybrid meshes which were used for Martin&Leishman's blade geometries do not have any symmetry boundary condition.

Symmetry boundaries are used to reduce the extent of the computational model to a symmetric subsection of the overall physical system [12]. There is no flux of all quantities across a symmetry boundary. The symmetry boundary condition can therefore be summarized as zero normal velocity at a symmetry plane and zero normal gradients of all variables at a symmetry plane. Since the shear stress is zero at a symmetry boundary, it can also be interpreted as a "slip" wall when used in viscous flow calculation [12].

6.5 Wall Boundary Conditions

Wall boundary condition was used for the blade geometries. In all of the cases that were considered in this study, the no-slip boundary condition was enforced at walls. Also, Fluent provides to the user to specify a tangential velocity component in terms of the translational or rotational motion of the wall boundary, or model a "slip" wall by specifying shear. For no-slip wall conditions, Fluent uses the properties of the flow adjacent to the wall/fluid boundary to predict the shear stress on the fluid at the wall [12].

7. RESULTS

The three-dimensional flow fields around the helicopter rotor blades were investigated in hover flight. In this section the different rotor configuration are considered. Caradonna and Tung [4] rotor is used for validation. After the validation of rotor the airfoil was changed to VR7 to compare the two blades which have the same properties except airfoils. Then, the last step of this study was to show how the blade-tip configurations affect the performance of the rotor.

7.1 Validation

Caradonna and Tung Rotor [4]

The blade is untwisted, and consists of a single airfoil, NACA0012. It has a rectangular planform with an aspect ratio equal to 6. It was analyzed in two different tip Mach numbers that were 0.439 and 0.877. The ratio between thrust coefficient and solidity was equal to 0.1. This blade was chosen to validate the computed data with experiment of Caradonna and Tung [4]. Structured grids are produced using in house available software for the analysis. Spalart-Allmaras [12] and Spalart-Allmaras DES [12] turbulence models are used to account for the turbulence effects.

Four blade stations at which the comparisons are made are shown in Figure 7.1. (r/R 0.50, 0.68, 0.80, and 0.96).

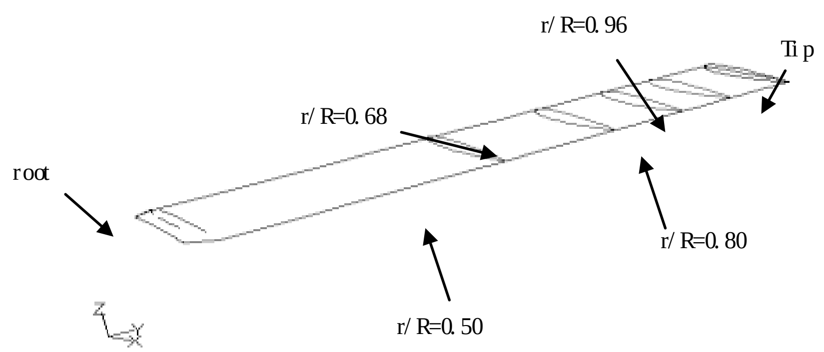

Figure 7.1 Four blade stations of Caradonna &Tung's rotor at where the results are presented

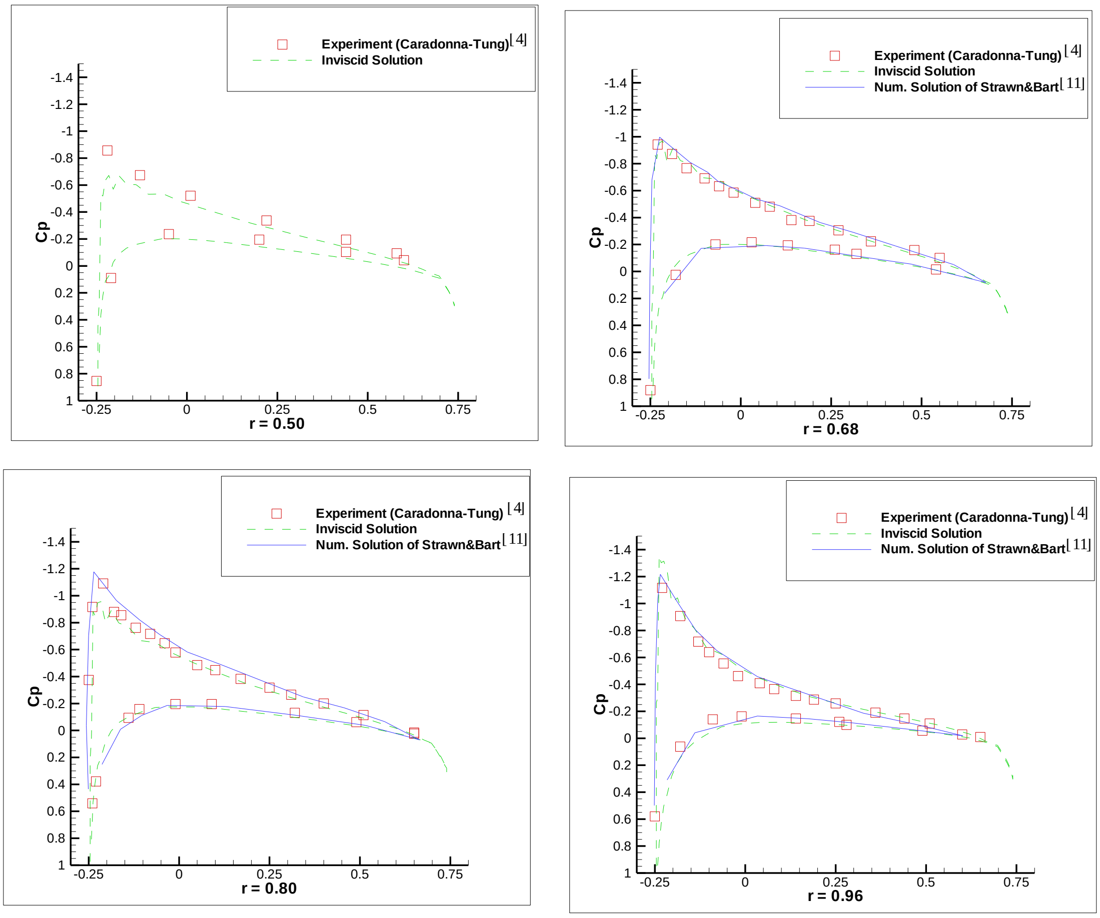

Figure 7.2 Pressure distributions for four sections of Caradonna &Tung [4] rotor in comparison with the numerical results of Strawn&Bart [11] and experimental data of Caradonna &Tung's [4] for Euler solution (M_t=0.439, θ_c =8^0)

Figure 7.2 shows the pressure coefficients for the low speed case, M_t=0.439. In the inviscid solution case, good agreement is seen between the numerical and experimental values at all locations, although the thrust value is slightly higher than the experimental one. It appears that the vortex-induced downwash needs to be higher in order to have better agreement with data [11].

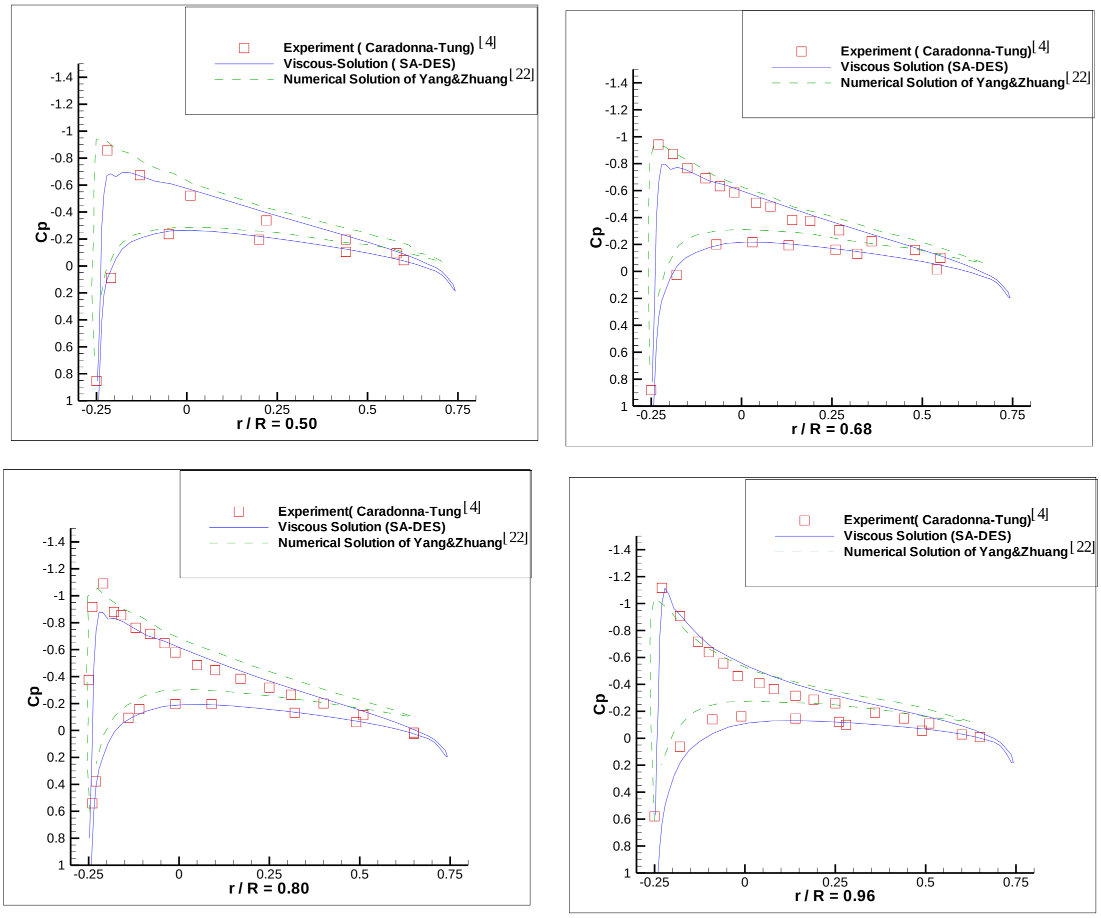

Figure 7.3 Pressure distributions for four sections of Caradonna &Tung [4] rotor in comparison with the numerical results of Yang &Zhuang [22] and experimental data of Caradonna &Tung [4] for Navier-Stokes solution (M_t=0.439, $\theta_c=8^0$)

It can be seen from Figure 7.3 that the surface pressures for the viscous solution have lower peak at the leading edge. This is probably due to coarse grid. Another fact is that near the rotor tip the calculated loading without vortex modeling still matches well with the experimental data. The loading at the blade-tip region is dominated by three dimensional tip effects and is relatively insensitive to the rotor trailing vortex [22].

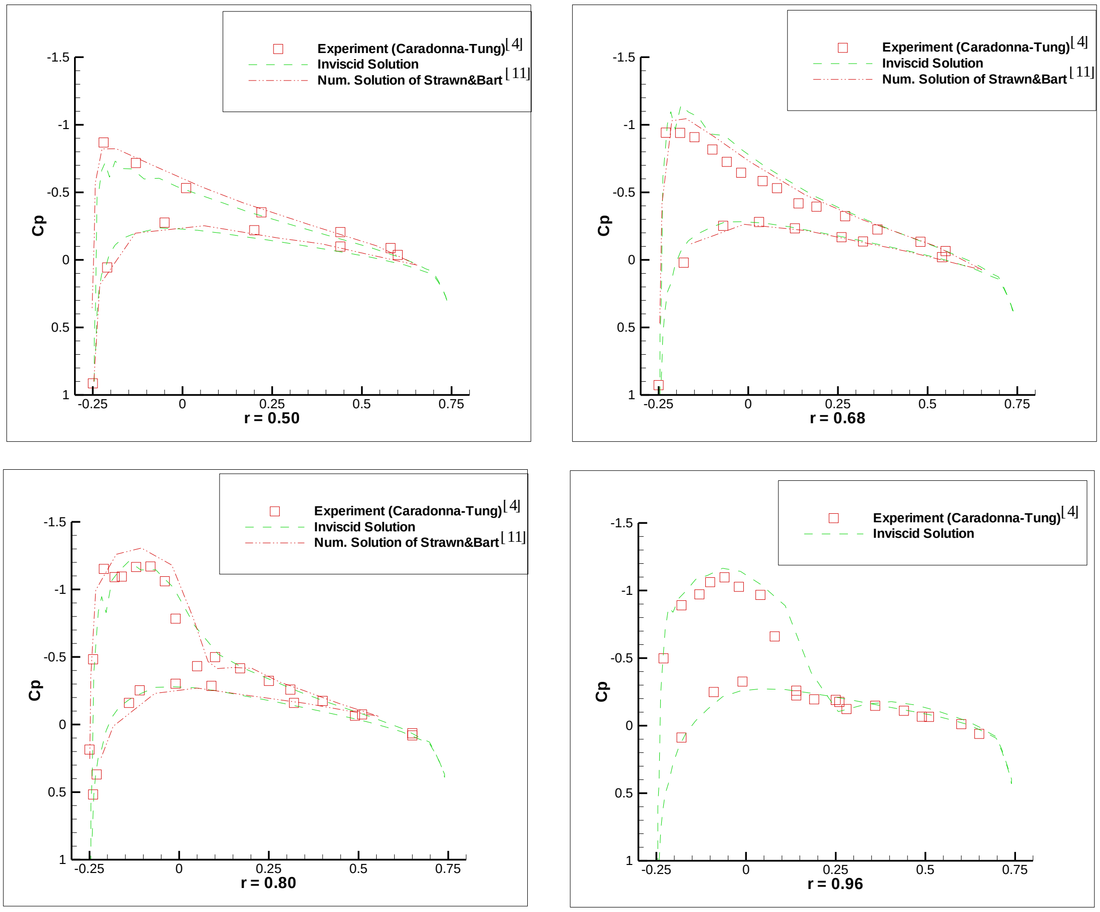

Figure 7.4 Comparison of surface pressures for a lifting rotor in hover for Euler solution (M_t=0.877, $\Theta_c=8^0$)

The blade tip velocity was increased to M_t=0.877 and then the same procedures were applied for this analysis. The surface pressures for the high speed case are shown in Figure 7.4. Good agreement is seen between numerical and experimental results. However, the predicted shock location at r/R 0.80 and r/R 0.96 is aft of the measured values. This is probably due to coarseness of the grid.

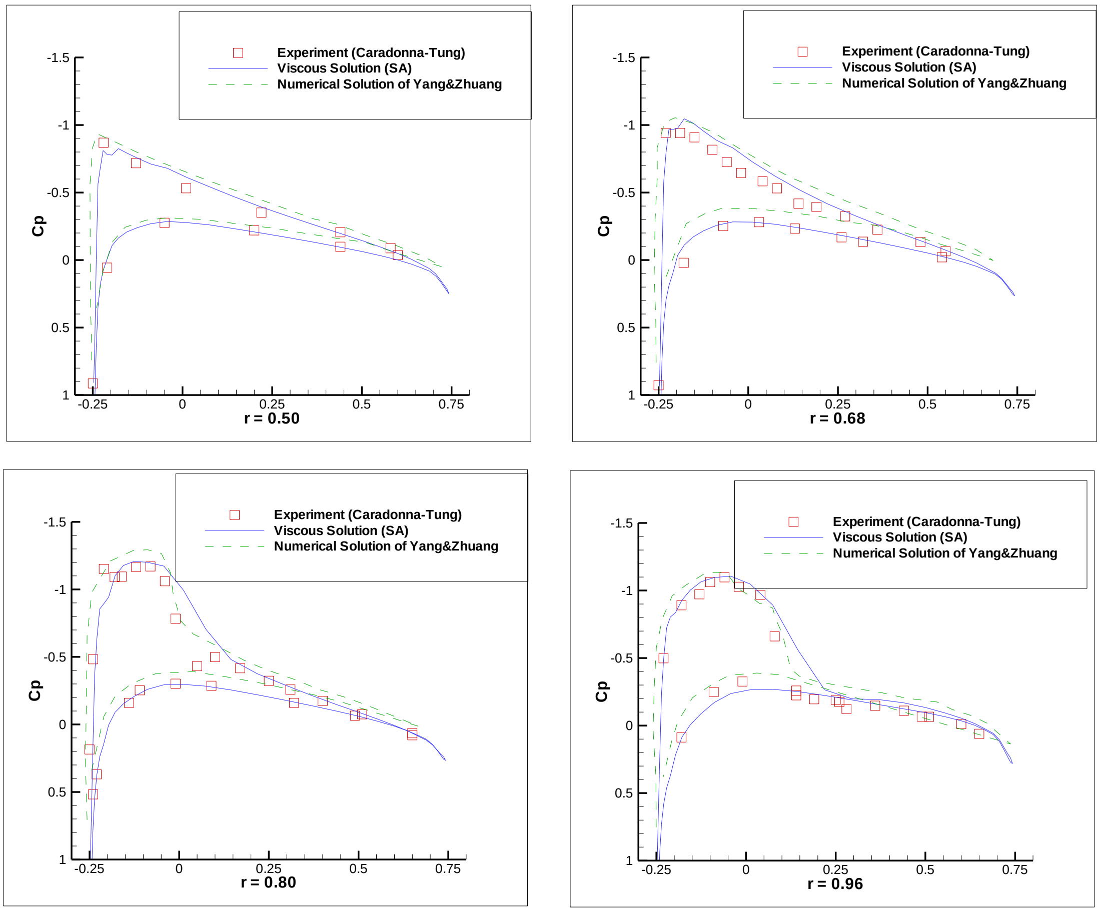

Figure 7.5 Comparison of surface pressures for a lifting rotor in hover for Navier-Stokes solution ($M_t=0.877$, $\theta_c=8^0$)

Figure 7.5 presents a final measure of computed performance results. The pressure distributions for four sections of Caradonna &Tung [4] rotor were compared with the numerical results of Yang &Zhuang [22] and experimental data of Caradonna &Tung [4].

The tip vortex evolution is also investigated. At the 0^0 azimuth, the blade is passing over the vortex from the preceding blade for the first time. This the location where the vortex trajectory and strength have the most influence on the blade air loads [11].

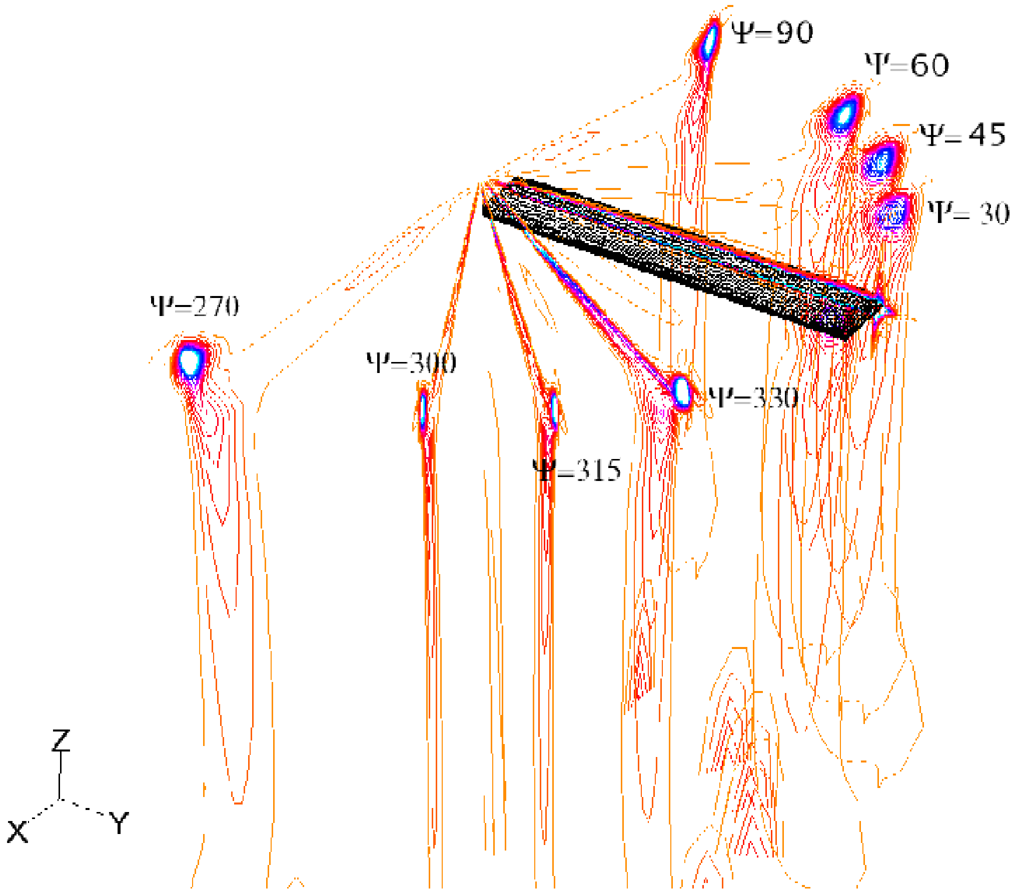

Figure 7.6 Vortex Core (M_t =0.439)

Vorticity contours are illustrated at different azimuth angles for M_t=0.439. The vorticity contours are shown in two-dimensional slices and the angular locations are indicated in Figure 7.6.

7.2 Generic Rotor with VR7 Airfoil

The blade is also untwisted, and consists of a single airfoil, VR7. It has a rectangular planform with an aspect ratio equal of 6. It was analyzed in two different tip Mach numbers (M_t=0.877 and 0.439) and collective angles ($\theta_c = 8^0 \, and \, 0^0$). Structured grids are produced using in house available software for the analysis. Spalart-Allmaras [12] and Spalart-Allmaras DES [12] turbulence models are used to account for the turbulence effects. There is no experimental data for this blade geometry so the initial thrust coefficients are taken from commercial code, Flight Lab. Thrust Coefficients for Blade with VR7 profile are;

Table 7.1 Thrust Coefficients for Blade with VR7 Profile

	M_t =0.439	M_t =0.877
$\theta_c = 0^0$	C_t =0.0005355	C_t =0.000625
$\theta_c = 8^0$	C_t =0.00735	C_t =0.00785

.

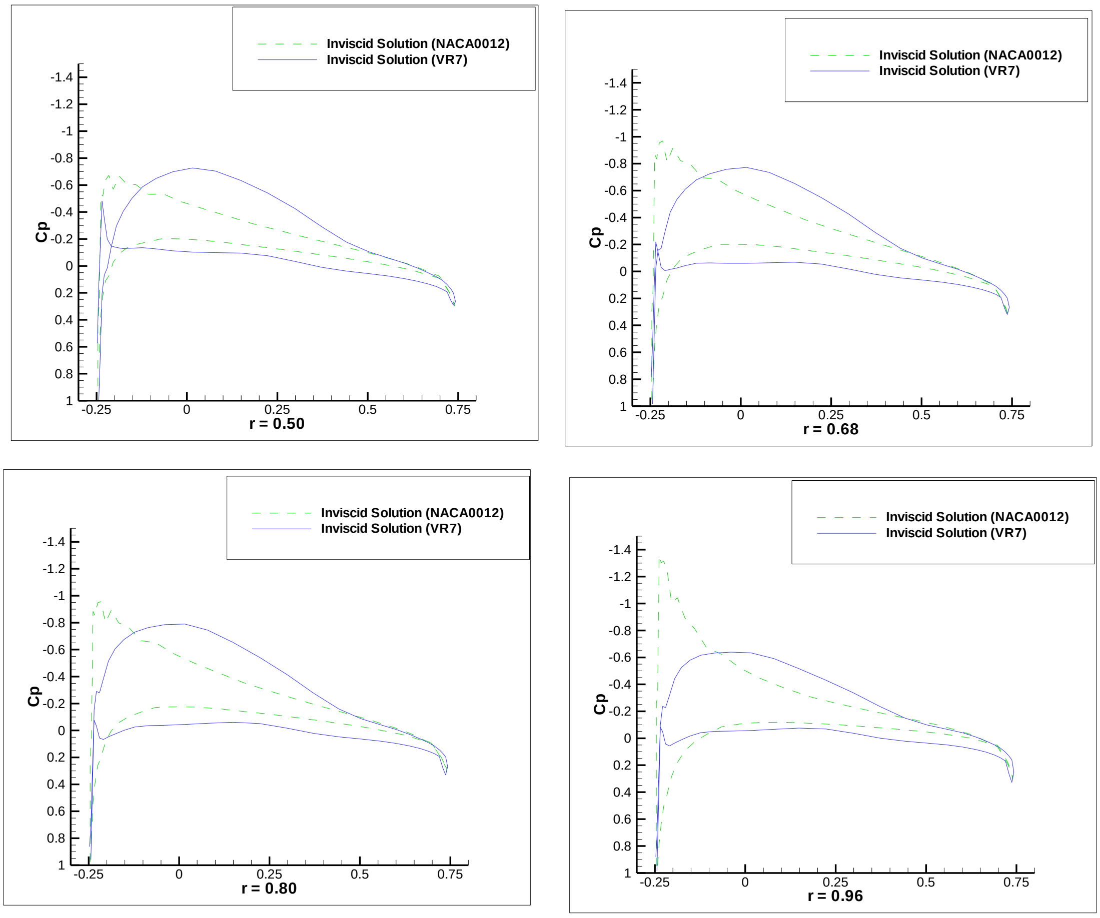

Figure 7.7 Pressure distributions for four sections of the generic rotor with single airfoil VR7 in comparison with the numerical results of Caradonna &Tung [4] rotor. (M_t=0.439, Θ_c =8^0)

Four blade stations were taken on the blade (r/R 0.50, 0.68, 0.89, and 0.96). Figure 7.7 shows the comparison of Euler results of Generic rotor and Caradonna&Tung [4] rotor.

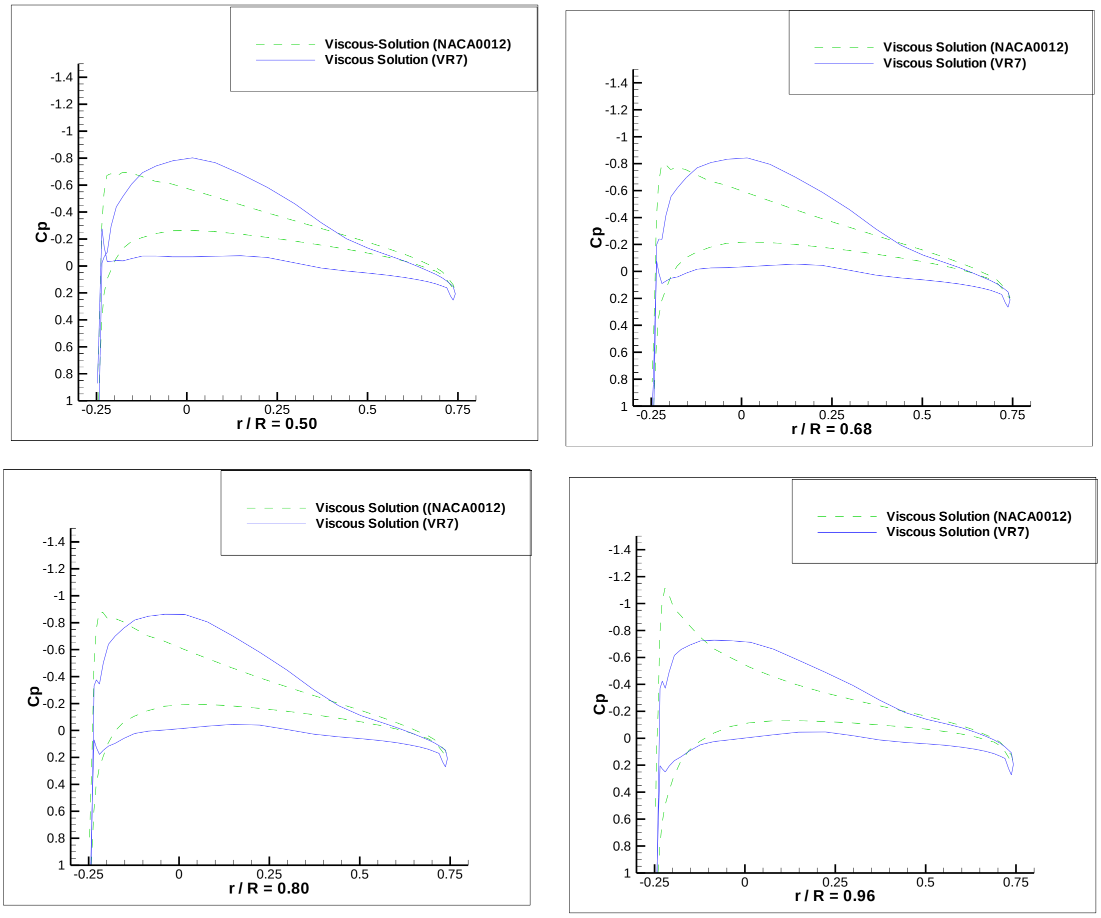

Figure 7.8 Pressure distributions for four sections of the generic rotor in comparison with the numerical results of Caradonna &Tung rotor [4]
(M_t=0.439, $\Theta_c=8^0$)

Then, the calculations of the Navier-Stokes equations with appropriate turbulence modeling were done for generic rotor and Caradonna &Tung [4] rotor.

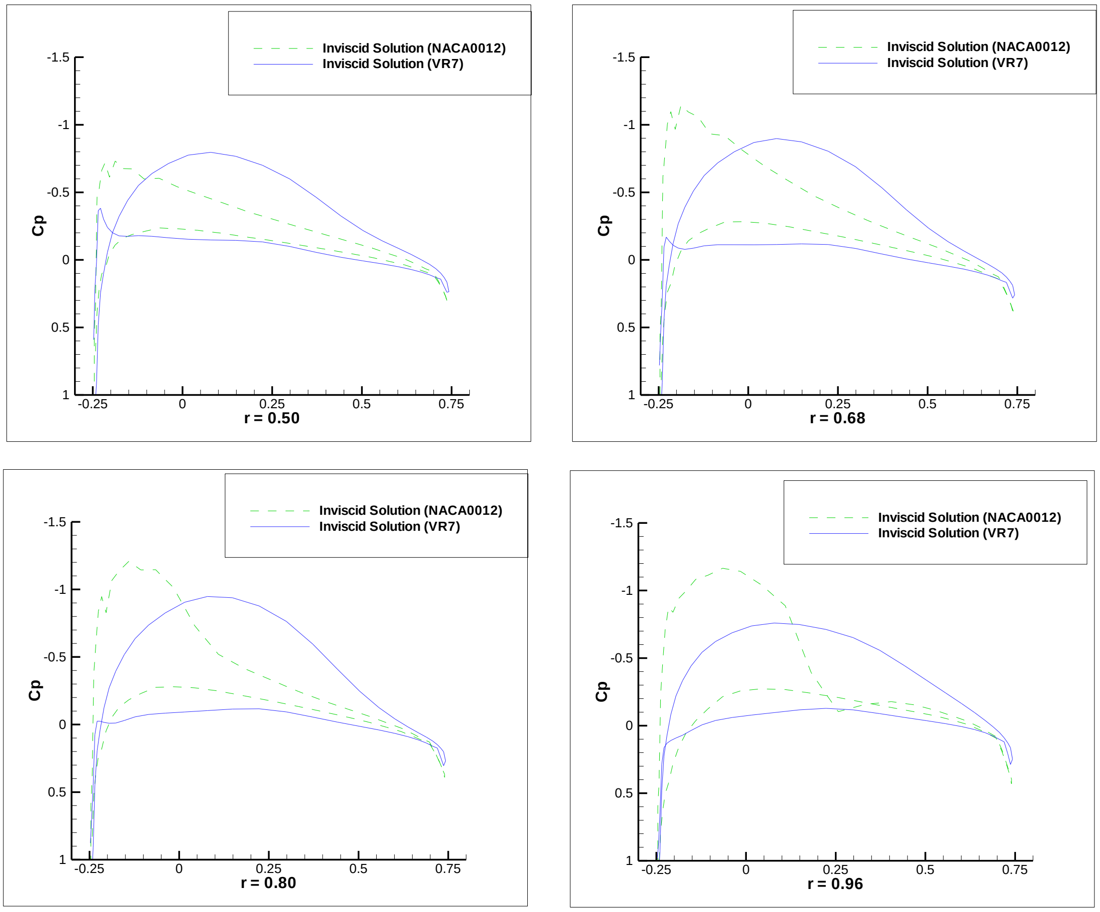

Figure 7.9 Chordwise pressure distributions at four radial stations of generic rotor in comparison with the numerical results of Caradonna & Tung [4] rotor (M_t=0.877, Θ_c=8^0)

To understand the effect of the blade tip speed, Mach number of tip speed was increased to 0.877 and then the same procedures were applied for these analyses. The comparison of pressure coefficients was illustrated in Figure 7.9.

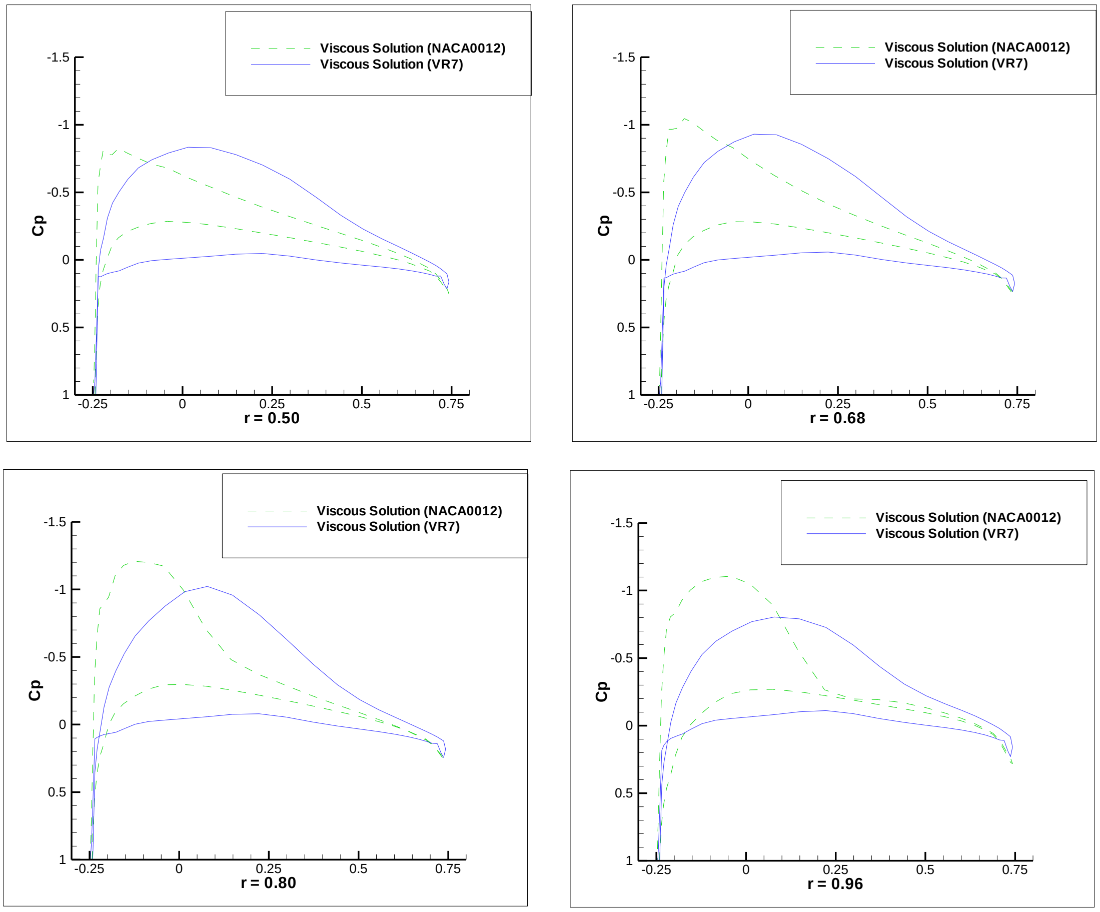

Figure 7.10 Comparison of surface pressures at different spanwise locations for the lifting rotors in hover (M_t=0.877, Θ_c =8^0)

Comparisons of surface pressure at those spanwise locations for the rotors are presented in Figure 7.10.

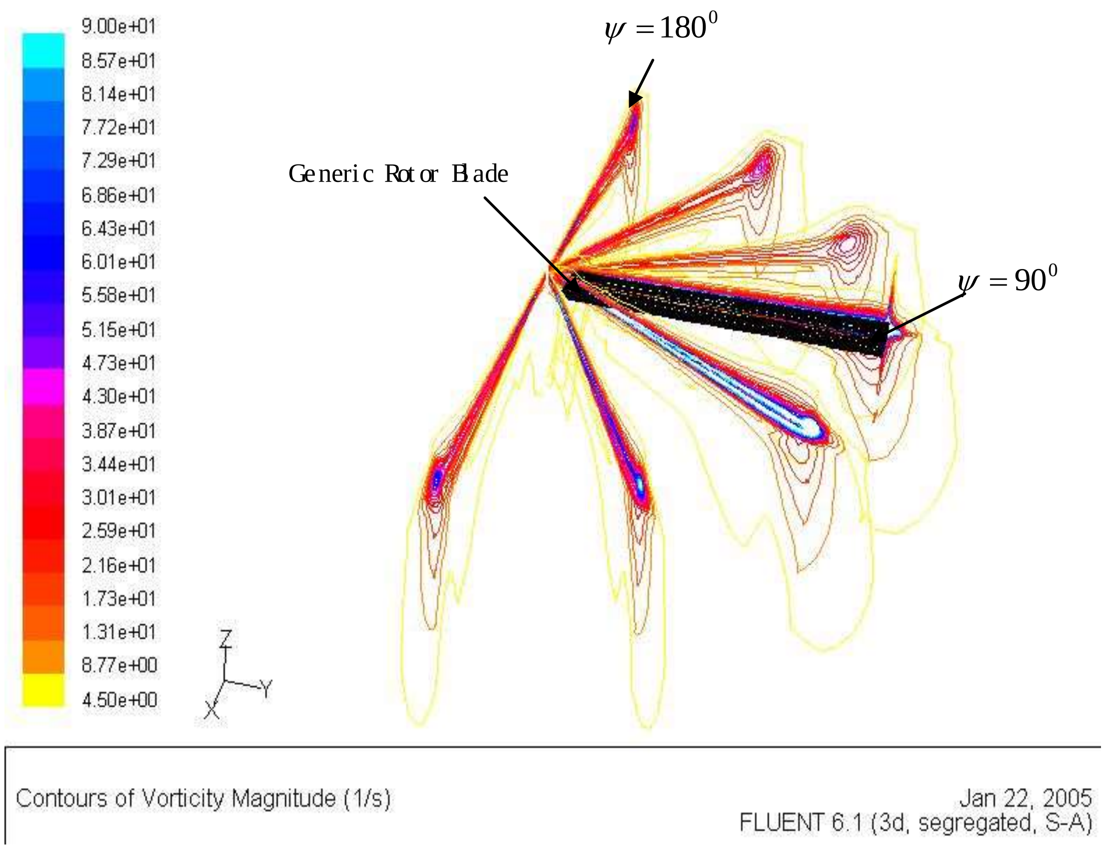

Figure 7.11 Vortex Core (M_t=0.877)

The tip vortex evolution is also examined in this study. Vorticity contours for the case are illustrated at different azimuth angles for M_t=0.877. The vorticity contours are shown in two-dimensional slices in Figure 7.11.

7.3 Effect of Tip Shape

The goal of this study was to investigate how the blade-tip configurations affect the performance of the rotor. Leishman and Martin [14] examined the wake aerodynamics of a single helicopter rotor blade with several tip shapes includes rectangular, swept and tapered. The blade parameters and test conditions are given in Table 5.1. In this work these three different rotors are simulated to examine the performance of each tip configuration. In these cases the overall grid was hybrid, since the grid consisted of both structured and unstructured parts. Calculated thrust values for these three blade configurations during this study converged to the experimental data and they were shown in Table 7.2. However, the major problem for these studies was the lack of the grid resolution after the structured part of the hybrid mesh. The tip vortices diffuse too quickly due to the coarseness of the grid. Solution adaptive grid refinement can be used to remedy this problem.

When the results are considered for the same tip mach number and collective pitch angle, it is seen that the swept tip rotor has more thrust and less drag than the baseline rotor blade, by the way; when tapered and swept tip blades are compared it's also seen that tapered one needs more collective pitch angle to produce nearly the same thrust.

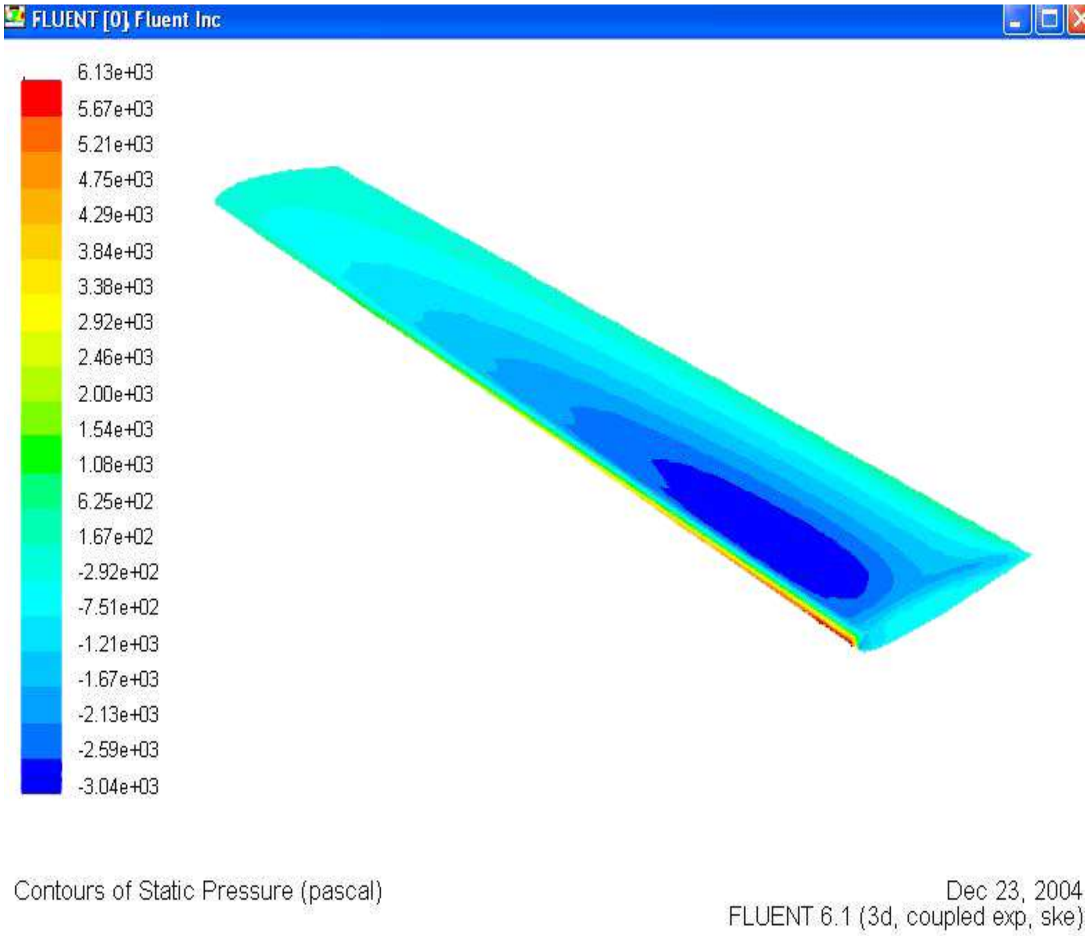

Figure 7.12 Static pressure distributions on baseline rotor of Leishman and Martin [14] (M=0.26)

First case of this study was the baseline rotor [14]. Static pressure distribution on baseline rotor of Leishman and Martin [14] is shown in Figure 7.12.

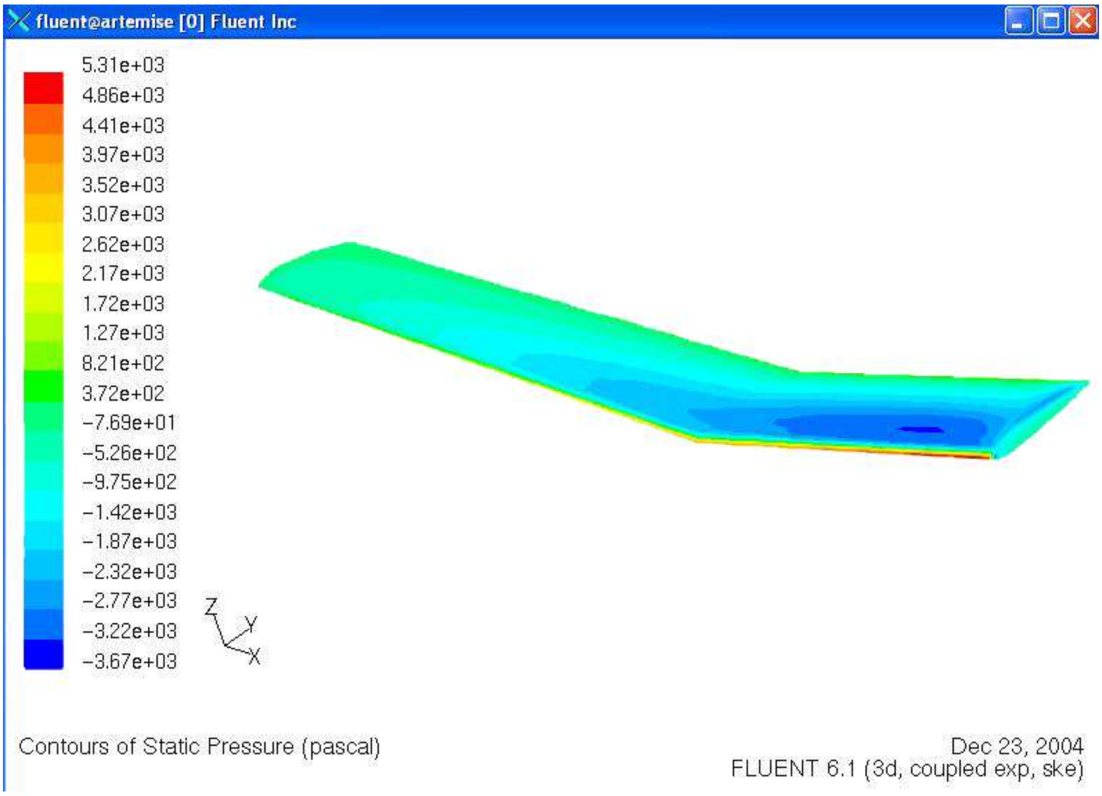

Figure 7.13 Static pressure distributions on swept tip rotor of Leishman and Martin [14] (M=0.3)

The planforms investigated in this case included a 20^0 swept tip that is shown in Figure 7.13.

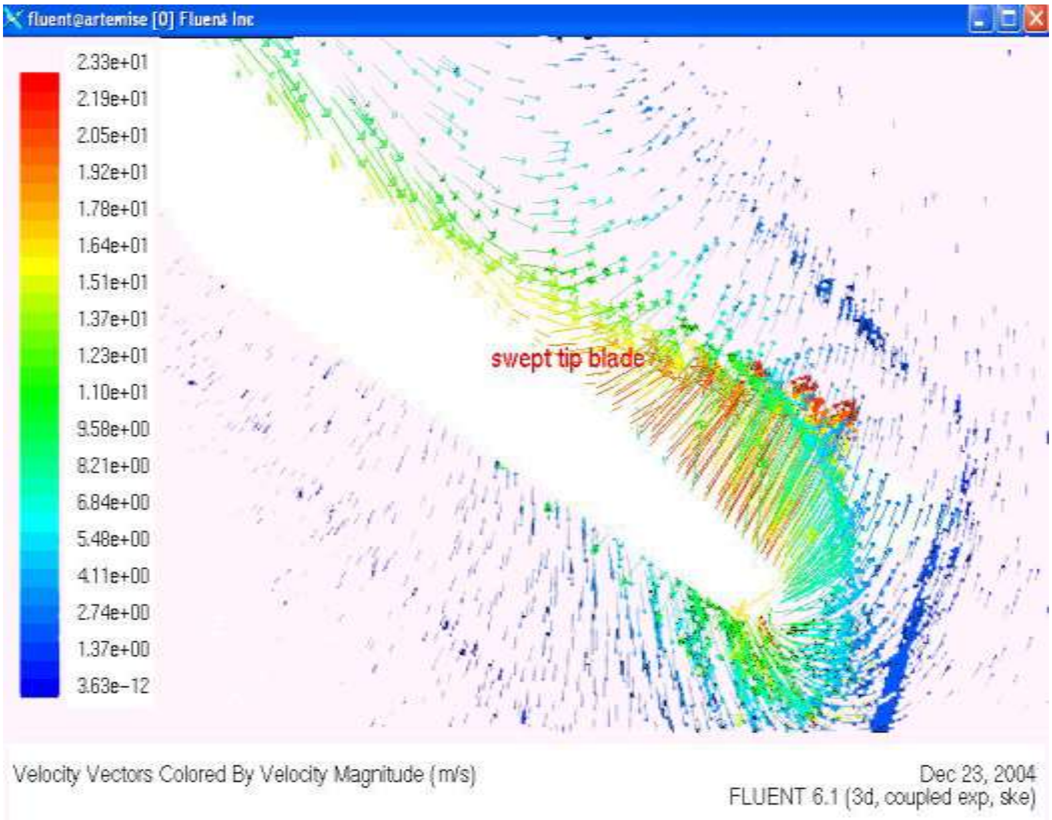

Figure 7.14 Velocity Vectors on swept tip rotor of Leishman and Martin [14] (M=0.3)

Velocity vectors on tip of the swept rotor are illustrated in Figure 7.14.

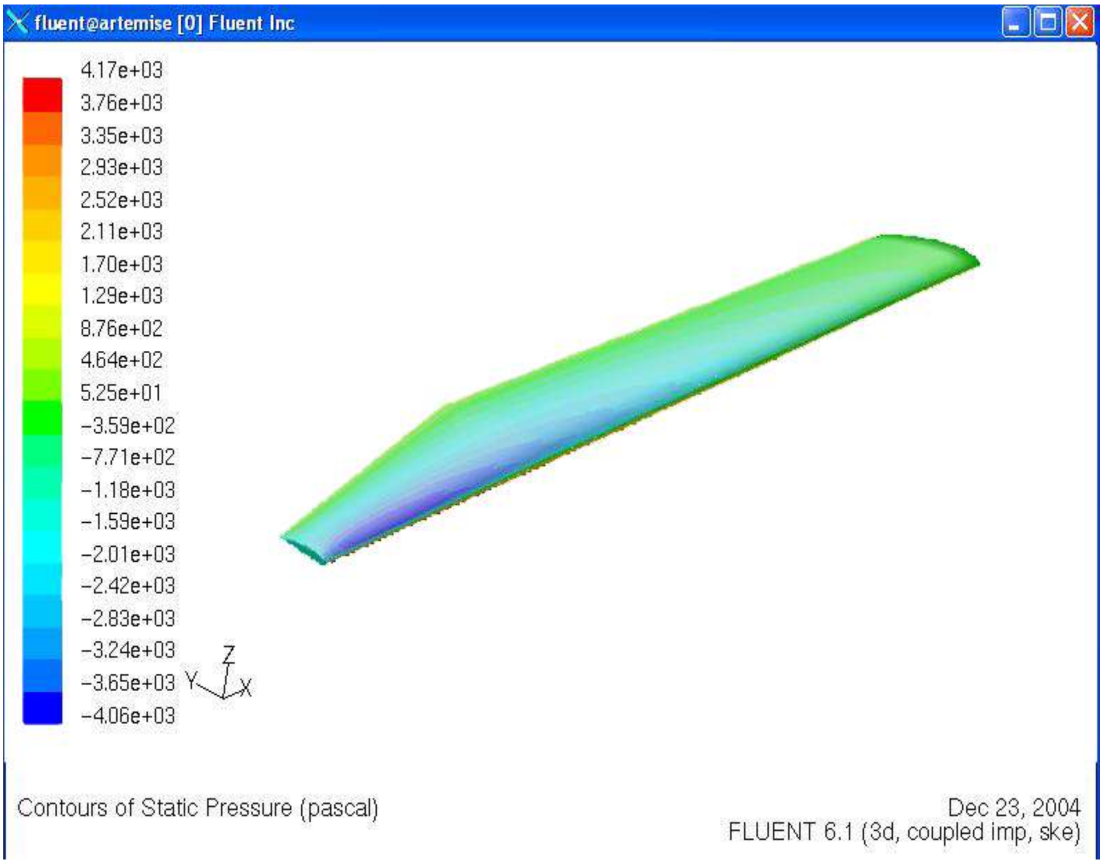

Figure 7.15 Static pressure distributions on tapered tip rotor of Leishman and Martin [14] (M_t=0.3)

The planforms examined in this study included a tapered blade with a 0.4 taper ratio. Figure 7.15 shows the static pressure distributions on tapered tip rotor.

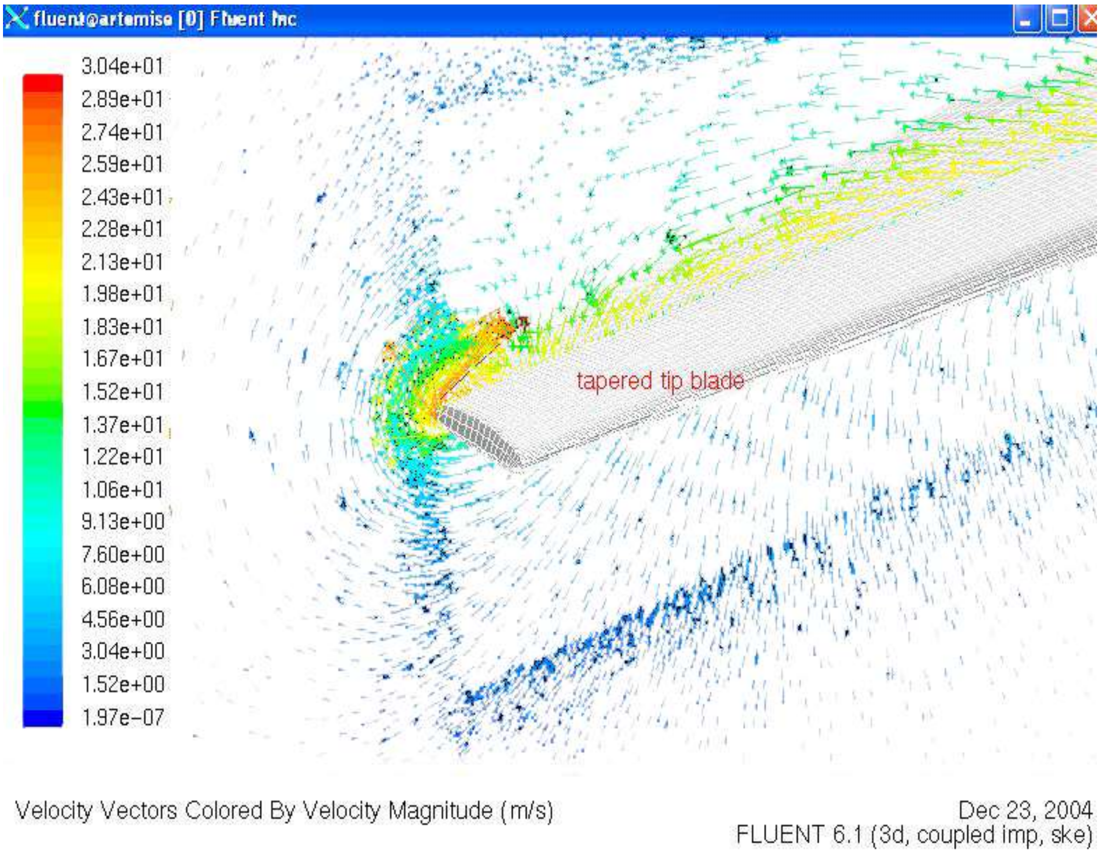

Figure 7.16 Velocity Vectors on tapered tip rotor of Leishman and Martin [14] (M=0.3)

Velocity vectors on the tip of the rotor blade can be seen in Figure 7.16.

Table 7.2 Results of All Blades Configuration

Tip Shape	Profile	Collective Pitch angle (^{0})	M_{tip}	C_T * 10^{-6} Experiment	C_T * 10^{-6} Present	C_D * 10^{-6} Present
Square	VR7	0	0.877	-	737	336
Square	VR7	0	0.439	-	720	349
Square	VR7	8	0.439	-	7800	1098
Square	VR7	8	0.877	-	8340	1090
Square	NACA0012	8	0.877	4565	5751	1381
Square	NACA0012	8	0.439	4565	5702	1318
Square	NACA2415	4.5	0.26	2200	2426	419
Tapered	NACA2415	6	0.3	2590	2488	331
Swept	NACA2415	4.5	0.3	2580	2510	382

Calculated thrust and drag coefficients for all blade configurations during this study are shown in Table 7.2. The results are more closely discussed in the following chapter.

8. CONLUSIONS

A commercial CFD code is used to compute the flowfield about different rotor blade geometries. The proximity far field boundary conditions obtained from blade element theory is externally fed into the solver, as a user defined function. Both inviscid and viscous flow solutions are obtained. The structured-unstructured grids are generated using both in house and commercial grid generators.

The methodology is first validated successfully using a six aspect ratio untwisted rectangular planform rotor blade consists of NACA0012 airfoil cross sections, for which experimental and various numerical results are available. Then the airfoil is changed to cambered, non-symmetric VR7 which is widely employed in rotorcraft applications. The blade with VR7 airfoil provides 36% more torque for the same angle of attack of 8 degrees for a tip Mach number of 0.44. This increase is 45% for a M_{tip}=0.88.

Finally, an attempt was made to study the effect of various tip shapes on rotor performance. The tapered and swept tip shapes are compared with that of rectangular one. Non-rectangular tip shapes seem to increase the performance by 10%. However, this study needs further analyses to fully clarify the effect of tip shapes on main rotor performance.

REFERENCES

[1] **Leishman J. G**, 2000. Principles of Helicopter Aerodynamics, Cambridge University Press, United Kingdom

[2] **Johnson W**, 1980. Helicopter Theory, Dover Publications, INC, New York

[3] **Kocurek, J. D and Tangler, J. L,** "A prescribed Wake Lifting Surface Hover Performance Analysis," Journal of the American Helicopter Society, Vol. 22, No. 1, January 1977, pp. 24-35.

[4] **Caradonna, F. X, and Tung, C**, ''Experimental and Analytical Studies of a Model Helicopter Rotor in Hover,'' NASA TM81232, Sept. 1981

[5] **Allen, C B**, ''Convergence of steady and unsteady formulations for inviscid hovering rotor solutions'' Int. J. Numer. Meth. Fluids 2003; 41:931-949

[6] **Kewin W Noonan, WT. Yeager, and Jeffrey D. Singleton**, ''Wind Tunnel Evaluation of a Model helicopter Main-Rotor Blade with Slotted Airfoils at the Tip'', NASA/TP- 2001-21126, December 2001

[7] **Prouty R W**, 1995. Helicopter Performance, Stability, and Control, Kriger Publishing Company, Malabar, Florida

[8] http://www.helicopterpage.com/, 2004

[9] http://www.centennialofflight.gov/essay/Dictionary/heli_rotor_systems/DI53 2004

[10] http://www.thaitechnics.com/helicopter/heli_principle.html, 2004

[11] **Strawn, R C, and Barth, J. T**, ''A Finite-Volume Euler solver for Computing Rotary- Wing Aerodynamics' on Unstructured Meshes'' 48th Annual forum of the American Helicopter Society, Washington, Dc, June 3-5, 1992

[12] Fluent 6.1 Tutorials

[13] **F. Caradonna**, ''Performance Measurement and Wake Characteristics of a Model Rotor in Axial Flight'' AHS Technical Specialists Meeting for Rotorcraft Acoustics and Aerodynamics, VA Oct., 1997

[14] **Preston B. Martin, and J. Gordon Leishman**, ''Trailing Vortex Measurements in the Wake of a Hovering Rotor Blade with various Tip Shapes'' 58th Annual forum of the AHS International, Montreal Canada, June 11-13, 2002

[15] **Shenoy, K. R. and Gray, R. B.,** "Iterative Lifting surface method for thick bladed hovering helicopter rotors," Journal of Aircraft, Vol. 18, No. 6, June 1981, pp. 417-424.

[16] **Bhagwat, M.J, and Leishmann J. G**, Correlation of helicopter rotor tip vortex measurements. AIAA Journal, Vol. 38, No. 2, pp 301-308, 2000.

[17] **Leishman J. G, and Bagai A**, Challenges in understanding the vortex dynamics of helicopter rotors. AIAA Journal, Vol. 36, No. 7, pp 1130-1140, 1998.

[18] **Vuillet A**, Rotor and blade aerodynamic design. Aerodynamics of rotorcraft. AGARD report No. 871, pp3-1, 3-59, and 1990.

[19] **Martin PB and Leishmann JG**, Trailing vortex measurements in the wake of a hovering rotor blade with various tip shapes. 58th Annual Forum of the AHS International, Montreal Canada, June 11-13, 2002.

[20] **Srinivasan GR, Raghavan V, and Duque EPN**, Flow field analysis of modern helicopter rotors in hover by Navier-Stokes Method. Presented at the International Technical Specialists Meeting on Rotorcraft Acoustics and Rotor Fluid Dynamics, Philadelphia, PA, Oct. 15-17, 1991.

[21] Gridgen V15.02 Tutorial, 2003.

[22] **Yang G, and Zhuang L.,** Numerical Simulation of Rotor Flow in Hover, Journal of Aircraft, Vol. 37, No.2, March-April 2000

[23] **Gray, R. B**, "On the Motion of the Helical Vortex Shed from a single bladed Hovering Model rotor and its Application to the calculation of the spanwise aerodynamic loading," Princeton University Aero. Engineering Department, Report No. 313, September 1955.

[24] **Landgrebe, A. J. and Cheney, M. C**, "Rotor Wakes - Key to Performance Prediction," AGARD Conference on Aerodynamics of Rotary Wings, AGARD-CPP-111, February 1973

[25] **Scully, M. P.,** "Computation of Helicopter Rotor Wake geometry and its influence on Rotor Harmonic Airloads," MIT, ASRL-TR-178-1, March 1975

[26] **Summa, J. M.** "Potential Flow about three-dimensional lifting configurations, with applications to wings and rotors," AIAA paper 75-125, 1975.

[27] **Bliss, D B and Miller, W O,** " Efficient free wake calculations using analytical/numerical matching and far-field linearization, " presented at the 45th Annual American Helicopter Society Forum, Boston, MA, May 1989

[28] **Johnson, W,** "A Comprehensive Analytical Model of Rotorcraft Aerodynamics and Dynamics,'' NASA TM 81182, 1982

[29] **Caradonna, F. X and Isom, M. P.**, "Subsonic and Transonic Potential Flow over Helicopter Rotor Blades, AIAA Journal, No. 12, December 1972, pp. 1606-1612.

[30] **Chang, I. C**, "Transonic Flow Analysis for Rotors,'' NASA TP 2375, July 1984.

[31] **Wake, B E and Sankar, L N**, "Solution of Navier-Stokes equations for the flow over a rotor blade ", Journal of the American Helicopter Society, April 1989.

[32] **Mello, O A F.,** "An Improved Hybrid Navier-Stokes/Full Potential Method for Computation of Unsteady Compressible Flows, " Ph. D Thesis, Georgia Institute of Technology, Atlanta, GA, Novermber 1994.

[33] **Berezin, C R and Sankar, L N,** "An Improved Navier-Stokes/Full Potential Coupled Analysis for Rotors, " Mathematical Computational Modelling, Vol. 19, No. 3/4, 1994, pp. 125-133.

[34] **Moulton, M A, Hafez, M M and Caradonna, F. X,** "Zonal procedure for predicting the hovering performance of a helicopter,'' ASME Journal, Vol. 184, 1984.

[35] **Tang, L**, ''Improved Euler Simulation of Helicopter Vortical Flows,'' Ph. D Thesis, University of Maryland, 1998

APPENDIX A

UDF is a function that you program that can be dynamically loaded with the FLUENT solver to enhance the standard features of the code. UDFs are written in the C programming language. They are defined using DEFINE macros that are supplied by Fluent Inc. They access data from the FLUENT solver using predefined macros and functions also supplied by Fluent Inc [12]. UDF which is used in this work is given below

```
#include "udf.h"
#define Mt 0.439                                  /* blade tip velocity */
#define Ct 0.004565                               /* rotor thrust coefficient */
#define R 6.0                                     /* blade radius */
#define ses_hizi 340                              /* speed of sound*/
#define merkez_x 0.0                              /* center coordinate*/
#define merkez_y 0.0
#define merkez_z 0.0
DEFINE_PROFILE (velocity_x, thread, position)     /* Fluent Macro*/
 real point[ND_ND];                         /*this will hold the position vector */
  face_t f;                                 /*face knowledge */
  real x,y,z;                               /* center coordinates of face..*/
  real r=0.0;                               /*the distance between hub and boundary face*/
  real s=0.0;
  real teta,fi;                             /* coordinate angles*/
  real c=0.0;
  real sonuc1=0.0;
  begin_f_loop (f, thread)                  /*for all faces...*/
  {
     F_CENTROID(point, f, thread);          /*finds the center of face */
     x=point[0]; y =point[1]; z=point[2];
  r=sqrt ((merkez_x-x)*(merkez_x-x) +(merkez_y-y)*(merkez_y-y) +(merkez_z-z)*(merkez_z-z));
```

```
 fi=acos((z-merkez_z)/r);
          teta=atan2((x-merkez_x),(y-merkez_y));
 c=((-1*M*.25)*(sqrt(G*.5))*((R/r)*(R/r))); .........................................................................( Equation 4.26)
 s=sin(fi)*c;
sonuc1=cos((teta))*s;
          F_PROFILE(f, thread, position)=sonuc1*ses_hizi;
  }
 end_f_loop (f, thread)
}
DEFINE_PROFILE(velocity_y,thread,position)
{ real point[ND_ND];
 face_t f;
 real x,y,z;
 real r=0.0;
 real s=0.0;
 real teta,fi;
 real c=0.0;
 real sonuc2;
 begin_f_loop(f, thread)
 {
   F_CENTROID(point,f,thread);
   x=point[0]; y =point[1]; z=point[2];
          r=sqrt((merkez_x-x)*(merkez_x-x)+(merkez_y-y)*(merkez_y-y)+(merkez_z-z)*(merkez_z-z));
          fi=acos((z-merkez_z)/r);
          teta=atan2((x-merkez_x),(y-merkez_y));
          c=((-1*M*.25)*(sqrt(G*.5))*((R/r)*(R/r))); ..........................................................( Equation 4.26)
          s=sin(fi)*c;
          sonuc2=sin((teta))*s;
F_PROFILE(f, thread, position)=sonuc2*ses_hizi;
  }
 end_f_loop(f, thread)
}
```

```
DEFINE_PROFILE(velocity_z,thread,position)
{ real point[ND_ND];
  face_t f;
  real x,y,z;
  real r=0.0;
  real fi;
  real c=0.0;
  real sonuc3;
  begin_f_loop(f, thread)
  {
     F_CENTROID(point,f,thread);
     x=point[0]; y =point[1]; z=point[2];
          r=sqrt((merkez_x-x)*(merkez_x-x)+(merkez_y-y)*(merkez_y-y)+(merkez_z-z)*(merkez_z-z));
          fi=acos((z-merkez_z)/r);
          c=((-1*Ml*.25)*(sqrt(Gt*.5))*((R/r)*(R/r))); ...............................................................( Equation 4.26)
          sonuc3=cos((fi))*c;
          F_PROFILE(f, thread, position)=sonuc3*ses_hizi;
   }
  end_f_loop(f, thread)
}
```

RESUME

Bedri Yağız was born in Adana in 1979. After graduating from G Antep Vehbi Dinçerler Fen Lisesi in 1997, he started his under graduate study at Istanbul Technical University, Department of Aeronautics in same year. He graduated from this department in 2002. The following year, he was accepted to Advanced Technologies in Aeronautics and Astronautics Engineering programme of Graduate Institute of Istanbul Technical University.